

This is the preprint version of the contribution published as:

Li, T., **Schlüter, S.**, Dragila, M.I., Wildenschild, D. (2018):
An improved method for estimating capillary pressure from 3D microtomography images and
its application to the study of disconnected nonwetting phase
Adv. Water Resour. **114**, 249 - 260

The publisher's version is available at:

<http://dx.doi.org/10.1016/j.advwatres.2018.02.012>

An Improved Method for Estimating Capillary Pressure from 3D Microtomography Images and its Application to the Study of Disconnected Nonwetting Phase

Tianyi Li¹, Steffen Schlüter², Maria Ines Dragila³ and Dorte Wildenschild^{1,*}

¹ School of Chemical, Biological, and Environmental Engineering, Oregon State University

² Department of Soil System Sciences, Helmholtz Centre for Environmental Research, Halle, Germany

³ Department of Crop and Soil Sciences, Oregon State University

* corresponding author

Abstract

We present an improved method for estimating interfacial curvatures from x-ray computed microtomography (CMT) data that significantly advances the potential for this tool to unravel the mechanisms and phenomena associated with multi-phase fluid motion in porous media. CMT data, used to analyze the spatial distribution and pressure-saturation (P-S) relationships of liquid phases, requires accurate estimates of interfacial curvature. Our improved method for curvature estimation combines selective interface modification and distance weighting approaches. It was verified against synthetic (analytical computer-generated) and real image data sets, demonstrating a vast improvement over previous methods. Using this new tool on a previously published data set (multiphase flow) yielded important new insights regarding the pressure state of the disconnected nonwetting phase during drainage and imbibition. The trapped and disconnected non-wetting phase delimits its own hysteretic P-S curve that inhabits the space within the main hysteretic P-S loop of the connected wetting phase. Data suggests that the pressure of the disconnected, non-wetting phase is strongly modified by the pore geometry rather than solely by the bulk liquid phase that surrounds it.

Keywords: Multiphase flow, Porous media, Computed microtomography, Curvature, Capillary pressure measurement.

1. Introduction and Background

Systems involving multi-phase flow in porous media are encountered in many different technical fields of interest to society, including environmental engineering, hydrogeology, agriculture, and petroleum engineering. For a several decades now, x-ray computed microtomography (CMT) has made it possible to visualize and quantify microscale characteristics associated with interfacial properties and fluid distributions of relevance to multi-phase fluid systems in the subsurface. Consequently, image analysis of the resulting three-dimensional microtomographic image data has become an essential component of pore-scale investigations.

For analysis, original gray scale images generated by CMT are first filtered to reduce noise and then segmented into a number of phase classes via multiple algorithms such that all voxels belonging to an individual phase in the system (oil, water, solid) have the same integer value. The segmented data is typically used for a variety of measurements, but the resulting estimates are known to vary depending on the quality and fidelity of the original images, the precision of the segmentation processes, and appropriateness of the implemented measurement algorithms (*Porter and Wildenschild, 2010; Schlüter et al., 2014*). An important characteristic of flow in unsaturated porous media is the capillary pressure-saturation relationship. The connection between capillary pressure and fluid-fluid interfacial curvature expressed by the Young-Laplace (Y-L) equation, opens new avenues of exploration in pore-scale imaging and image analysis.

In the Young-Laplace equation,

$$P_c = \sigma \left(\frac{1}{r_1} + \frac{1}{r_2} \right) = 2K_{mean}\sigma \quad (1)$$

P_c is capillary pressure, r_1 and r_2 are the two orthogonal principal radii of curvature, K_{mean} is mean interfacial curvature, and σ is interfacial tension.

Two fundamentally different approaches exist for estimating the interface curvature from image data: **(1)** A voxel-based approach that uses the image intensity gradient, however curvature estimation using this method is associated with various limitations, and is highly sensitive to image quality (Bullard *et al.*, 1995; Thirion and Gourdon, 1995). **(2)** A surface-based approach, introduced by Armstrong *et al.* (2012a), that uses a triangulated surface generated from the segmented images to estimate curvature. The most commonly adopted approach for surface generation is the marching cubes algorithm (Lorensen and Cline, 1987). Although the surface-based approach is becoming more frequently used (Armstrong *et al.*, 2012b; Armstrong and Wildenschild, 2012; Andrew *et al.*, 2014; Armstrong *et al.*, 2014; Singh *et al.*, 2016 and Garing *et al.*, 2017), curvature estimates remain sensitive to various issues such as the amount of smoothing, segmentation accuracy, and image pixelation (e.g. Armstrong *et al.*, 2012a; and Garing *et al.*, 2017). Recent attempts to improve the accuracy of curvature estimation have mainly focused on image quality. Garing *et al.* (2017) for instance reported that variation in curvatures seen at 2x resolution (3.28 micron voxels) was absent at 4x resolution (1.62 micron voxels) for their glass bead samples. Yet, for their sandstone rock samples, there was variation in curvatures for disconnected phase at both the 2x and 4x resolutions. Two very recent studies by Herring *et al.* (2017) and Singh *et al.* (2017) employ techniques similar to what is presented here; Herring *et al.* based their approach directly on the work presented here, while Singh *et al.* applied dilation by a fixed number of voxels of their rock surfaces to achieve a similar approach to what we achieve with a percentage “clipping” of the interface near the solid surface.

Instead of focusing on increased image resolution, this paper introduces a more accurate method for curvature estimation. The improved algorithm is validated against synthetic data and real CMT data sets using measured capillary pressure values from a multi-phase flow drainage-imbibition experiment. Finally, the new method is used to gain insights into the evolution of the capillary pressure of a *disconnected* nonwetting phase trapped within a porous medium.

2. Materials and Methods

This section describes the different image processing approaches used for curvature estimation, and the experimental and synthetic data sets used for verification and testing of the new method.

2.1. Experimental data sets

The first (numerical) data set discussed is a series of computer-generated images of interface menisci within capillary tubes of different radii. These analytical configurations were used to validate the new curvature algorithm and quantify curvature estimation error. A hemisphere was generated within a column in order to create a perfect concave meniscus, then a grey scale image was generated, and the image analyzed using the same method as for CMT-obtained images. For these computer generated data sets, the theoretical mean curvature values for each data set is known, calculated as the reciprocal of the radius.

The second (real, CMT) data set was collected at the Advanced Photon Source, Argonne National Laboratory. The experimental system consisted of water-wet glass beads with a ratio of 35% 0.6 mm diameter, 35% 0.8 mm diameter, and 30% 1.0-1.4 mm diameter packed into a 25.0 mm long glass column with an inside radius of 3.5 mm (*Porter et al.*, 2010; *Armstrong et al.*, 2012a). The two phases used were Soltrol 220 (non-wetting phase, $\rho=0.79 \text{ g/cm}^3$, $\sigma=0.0378 \text{ N/m}$) and potassium iodide-doped water (wetting phase, 1:6 mass ratio of KI:H₂O, density = 1.17 g/mL). The non-wetting phase was connected to the top of the column, and the wetting phase was connected to the bottom of the column. A semi permeable hydrophilic membrane was placed at the bottom of the column to prevent the non-wetting phase from entering the water path. Pressure transducers connected to the oil and water lines (and referenced to the top of the sample) were used to externally record capillary pressures as the difference between wetting and nonwetting phase pressures. Wetting phase volume was controlled to $\pm 1 \text{ } \mu\text{L}$ by a syringe pump (Gilson 402). The system was first fully saturated with wetting phase, followed by primary drainage (PD) which nearly saturated the bead pack with oil, then main imbibition (MI), main drainage (MD), secondary imbibition (SI), and secondary drainage (SD) all referring to the wetting phase. For each drainage or imbibition, a varying, but precise (μL) amount of wetting phase was pumped out of (drainage) or into (imbibition) the system at a flow rate of 0.6 ml/hr

in a number of incremental steps. About 15 minutes were required for the fluids to reach quasi-equilibrium after each saturation change. We define quasi-equilibrium as a state where significant progress towards equilibrium has been made on a time-scale of minutes, but where complete equilibrium is not expected to be achieved for many hours, Gray et al. (2015) and Schlüter et al. (2017). Quasi-equilibrium was verified by checking the images; if fluids were still moving during the scan, the resulting images would be blurry. If that was the case, the sample would be rescanned after another 15 minute wait period. X-ray CMT images were obtained from a 5.5 mm section of the column at 13 μm /voxel resolution. All of the two-dimensional radiographs were preprocessed and reconstructed using algorithms developed by GeoSoilEnviro Consortium for Advanced Radiation Sources (GSECARS) (Rivers et al., 1999) to produce 3D volumes of data. Additional details about the experimental setup can be found in Porter et al. (2010).

2.2 Image Processing

All image processing was accomplished using the commercial software program Avizo Fire®. Segmentation is a necessary and crucial step that allows for subsequent accurate data analysis, and obviously relies heavily on the fidelity of the greyscale images. Generally, greyscale images are noisy and depending on how significant the noise is, it can negatively affect the quality of image segmentation. Hence, image filtering is commonly employed as a first step in image analysis. All the greyscale images in this work were subject to non-local means filtering to remove noise and blur, and then segmented using a watershed algorithm to render each phase to consist of a single label field.

2.2.1 Non-local means filter

Because of the particle nature of (synchrotron) light, shot noise (random variations in brightness) is prevalent in photon-counting optical devices, and x-ray based images are therefore inherently noisy. Due to its efficiency at noise removal (Buades et al., 2005), we applied a non-local means filter to the greyscale images. Based on trial, the search window, local neighborhood, and similarity value, which define the window size, the importance of each voxel in the window, and weighting factor, respectively, were set to 4, 7, and 3 voxels. As

shown in **Figure 1**, it was challenging to identify peaks and valleys in the original greyscale histogram. However, after applying the non-local means filter most of the noise is removed, leading to a sharper histogram with distinct peaks representing oil, water and beads, and an image that is much more homogeneous and significantly easier to segment.

2.2.2 Segmentation

Image segmentation is the process of classifying or dividing an image into different regions of voxels with similar greyscale intensity. Thus, the main goal of segmentation is to identify and convert a greyscale image into a simpler labeled image that is ready for subsequent analyses. For segmentation of the data presented here, we adopted the watershed segmentation as described by *Vincent et al.* (1991).

A recent study by *Schlüter et al.* (2014) compared various segmentation methods and concluded that the watershed algorithm was among the best for segmenting datasets of two-phase flow in porous media. A scan of the dry bead pack was used to identify the solid phase, which could then be superimposed on all other greyscale images. Relative to the analysis of *Armstrong et al.* (2012a), in the present analysis we also fixed some minor (and very local) segmentation artifacts. Using the watershed approach, the known regions in the data were initially identified by using a simple threshold. Next, the unknown transition regions, consisting of the points at the inflection between the two known phases, are allocated to one of the phases by analyzing the image intensity gradient. Eventually, the transitional regions will be minimized by the watershed module and labeled such that the 64000 greyscale values are sorted into only 3 classes: oil, water, and beads. Connected and disconnected wetting and non-wetting phases were distinguished using markers. This algorithm retrieves voxels in the image that are connected to a marker by using a 26 neighborhood connectivity requirement. A marker for connected non-wetting phase was placed on the top of the image (the oil reservoir was physically connected to the top of the sample) and a marker for connected wetting phase was placed at the bottom of the image (connected to the water reservoir). Therefore, the two fluid phases could be parsed into four configurations: connected wetting, connected non-wetting, disconnected wetting, and disconnected non-wetting. The interface between the connected

wetting phase and the connected non-wetting phase exerts a capillary pressure that can be measured by an externally placed pressure transducer. The connected phases, therefore, provide a basis for comparison between image-based estimates of capillary pressure and externally measured capillary pressures. In contrast, pressure of disconnected phases can not be measured externally. Therefore, accurately quantifying the interface geometry of disconnected fluid phases from tomographic images also provides us unprecedented insight into disconnected phase dynamics.

2.3 Surface generation

Three-dimensional surface generation was accomplished with the marching cubes algorithm (*Lorensen and Cline, 1987*) which approximates a smoothed interface between different phases using thousands of triangles. The number of triangles depends on the resolution of the input images, i.e., higher resolution results in more triangles. Once the image is segmented and labeled, the surface generation module in Avizo can be applied with different smoothing settings (type and extent). The surface generation module provides two smoothing options: constrained and unconstrained smoothing. Constrained smoothing guarantees that no label is altered during surface generation; any two voxel centers that have been labeled differently before the smoothing are separated by the generated surface afterwards. This is not necessarily the case for every small detail in the unconstrained case, and is therefore not considered in this work. Smoothing extent was studied in detail due to its parabolic characteristics and because selection of an appropriate value involves some trade-off; higher smoothing extent does not necessarily result in an improved, i.e., more accurate interface. Through careful evaluation of test spheres and capillary tubes, we found that constrained smoothing using a Gaussian filter, with a smoothing extent of 3 voxels, preserves the characteristics of the original data and provides adequate smoothing of the interface, which allows for greatest accuracy in the subsequent data analysis. In the interest of conciseness, the details of this separate investigation is not included here. We refer to Li (2015) for further details about the smoothing process.

2.4 Curvature Calculation

For a two-dimensional system, curvature is the inverse of the radius of an infinitely closely inscribed circle at a given point. In a three-dimensional shape, the normal vector and tangent vector are used to define the plane on which the curvature is calculated (**Figure 2**). All curves with the same tangent vector occupy the same normal vector. Taking into account all possible curvatures at a point on a surface, the maximum and minimum curvature values are called the principal curvatures, K_1 and K_2 , respectively. The mean curvature is then used to calculate capillary pressures by the Young-Laplace equation (Eq.1). The mean curvature is defined as half the sum of the principal curvatures, $K_{mean} = (K_1 + K_2)/2$. While the Gaussian curvature, which is the product of the principal curvatures ($K_1 \times K_2$), can also be used to extract details of interfacial geometry, it is not relevant for estimation of capillary pressures.

Capillary pressures estimated from surface-based curvature calculations suffer from errors introduced by limited image resolution along the triple line and physicochemical interactions near solid surfaces. No matter the image data size and resolution, the edge of the interface where oil and water connects near the solid surface will be rough, and this generates inaccurate curvature estimates in this region (**Figure 3**). *Armstrong et al.* (2012a) dealt with this problem by eliminating all positive curvatures values when calculating mean curvature (Method 2 in **Table 1**).

In this study, we propose a different methodology to increase the accuracy of the mean curvature estimate; the triangles that are close to the solid surface should either be given lower weight when generating the mean estimate, or be entirely eliminated from consideration based on their proximity to the solid surface. By doing so, mean curvature is estimated based primarily on segments of the interface that are not affected by their proximity to the solid surface. Each triangle is defined by three vertices as shown in **Figure 4a**. To accomplish this, we measure the shortest distance between each triangle's vertex and the solid surface (**Figure 4b**). The vertex distance calculation was performed based on Dijkstra's shortest edge distance algorithm (*Dijkstra*, 1959). The *shortest edge distance* of a triangle is calculated as the average of its three shortest vertex distances. Following the argument above, we introduce two new approaches that eliminate the effect of the solid surface on the curvature estimates.

220

221 2.4.1 Distance weighting

222 The shortest edge distance for each triangle is used as a weight factor to improve curvature
 223 calculations, by assigning more weight to triangles far from the solid surface and less to those
 224 that may be affected by the solid surface, see method 3 in Table 1. This so-called “distance
 225 weighted” mean curvature value for the interface ($K_{m,dw}$) is estimated based on the following
 226 equation:

$$227 \quad K_{m,dw} = \frac{\sum_i^N K_i D_i}{\sum_i^N D_i} \quad (2)$$

228 where the curvature value for each triangle (K_i) is multiplied by the triangle’s respective
 229 shortest edge distance (D_i).

230 2.4.2 Surface modification

231 Curvature estimates can also be improved by modifying the surface. A triangle is eliminated
 232 (the surface is clipped) if it is considered too close to the edge (solid surface), by determining if
 233 the *shortest edge distance* value is less than a chosen threshold (D_{min}). As an example, assume a
 234 threshold of 9.5 voxels, and two triangles with vertex distance values as shown in **Figure 5**. In
 235 this case the triangle on the left meets the requirement and will be preserved, whereas, the
 236 one on the right is eliminated from further consideration. Mean curvature and distance values
 237 for the preserved triangles are then used for generating surface modified mean curvature
 238 histograms (method 4 in Table 1).

$$239 \quad K_{m,sm} = (K_1 + K_2)/2 \quad for \quad D_i > D_{min} \quad (3)$$

240 Combining the distance weighted and surface modification methods (method 5 in Table 1),
 241 yields Equation 4.

$$K_{m,dw+sm} = \frac{\sum_i^N k_i D_i}{\sum_i^N D_i} \quad \text{for } D_i > D_{min} \quad (4)$$

The surface modification approach was validated using as a model, a numerically generated interface associated with a synthetic capillary tube, with an internal radius of 50 voxels. The theoretical mean curvature value of this meniscus is -0.02 voxel^{-1} (indicated by the red vertical line in **Figure 6a**). After testing of a range of threshold values, the shortest edge distance threshold (D_{min}) was set to 20% (in this case 20% of the 50 voxel radius). An example of the surface modification achieved using this approach is illustrated in **Figure 6b**, and ultimately, the successful match with the externally-measured (transducer) pressures confirms this choice. The resulting histograms for unmodified and modified interfaces (**Figure 6a**) illustrates that the curvature value after “surface-modification” clusters more narrowly around the theoretical value, but more importantly, the more positive values that are influenced by the solid surface have been successfully eliminated. For the real (CMT) data discussed later, the threshold was set to 20 percent of the maximum distance value for each data set, conceptually equivalent to 20% of a pore radii. In a very recent paper, Singh et al. (2017) used a similar approach by dilating the rock surfaces near the solid surface to eliminate interface voxels affected by the solid surface, however, they set their cutoff threshold to a fixed value of 4 voxels as they found that any further dilation affected the curvature values in a negative way. This is likely because they are working with rock samples with much finer features than the glass bead data used in this study, which contains larger pores and interfaces relative to the voxel resolution, and therefore leaves sufficient curvature behind, after a percentage clipping, to facilitate reliable curvature estimation. Herring et al. (2017) used an approach that follows our algorithm in terms of eliminating curvature measurements near the solid surface, and assigning higher weights to curvature measurements farther away from the solid surface. To achieve the desired accuracy for their more complex geometry (Bentheimer sandstone) with pore sizes approaching the image resolution, they included sub-voxel precise registration of the (Euclidian distance map of the) “dry” image to their partially-saturated volumes (both the segmented and grey-scale images).

3. Results

3.1 Testing the new curvature estimation method

The synthetic data set (menisci in capillary tubes of different radii) was used to test the accuracy of the five different methods described earlier and listed in **Table 1**. Because curvature estimation becomes tenuous for very small features, we expect to see significant improvement in the curvature estimates for larger radii tubes. The percentage errors listed in **Figure 7** are calculated as:

$$\text{Percentage error} = \left| \frac{\text{Measured value} - \text{Theoretical value}}{\text{Theoretical value}} \right| \quad (5)$$

It should be noted here that for a synthetic image, units do not really make sense, and the units can be referred to as voxels or microns, interchangeably. The results in **Figure 7** show that for the smallest capillary tube ($r = 10$ voxels), all methods introduce 9% or more error, however, as soon as the tube radius increases, we see a decrease in the error with increasing sophistication of the estimation method. For methods 1 and 2, i.e., using the entire data set, or negative values only, respectively, the error remains at 6% or more, regardless of the size of the capillary tube. Implementing the distance weighted algorithm (method 3) reduces the maximum error to below 5% for a radius of 25 μm , and approaches 1.5% for the largest tube. The surface modification (method 4) generates curvature estimates that are below 5% error at a capillary tube radius of 20 μm , and improves considerably, to only 3% error for the maximum radius tested. And finally, by combining distance weighting with surface modification (method 5), the decrease in error with increasing tube size is further enhanced, ending up at only 0.02% for the 55 μm tube. Clearly, combining these two new curvature estimation methods results in vast improvement over existing methods.

While the error calculated for a specific pore size decreases with increasing radii, natural porous media will present to the fluid a distribution of pore sizes. Therefore, a *characteristic accuracy* for each method, when applied to a media consisting of variously sized pores, is here calculated by the slope of the linear correlation between theoretical and measured curvatures

across all pore sizes tested (**Figure 8**). Note that a slope less than 1 signifies that all methods tend towards underestimating the curvature. As the methods march from #1 through #5, the slope approaches unity, thereby indicating improvement in accuracy with increasing sophistication of the estimation method.

Having successfully completed this method validation, we used the improved curvature estimation approach (method 5, Table 1) to analyze curvatures for the real (CMT) data set described earlier (*Porter et al.*, 2010), converting curvature estimates to capillary pressure (P_c) via the Young-Laplace equation, then comparing this image-based P_c to P_c measured using external pressure transducers.

In a previous study, *Armstrong et al.* (2012a) analyzed the data set from *Porter et al.* (2010) and demonstrated that by considering only *connected* fluid interfaces, and eliminating positive curvature values from consideration, transducer-based capillary pressure and curvature-based capillary pressure agreed surprisingly well for imbibition. However, the image-based measurement underestimated P_c relative to the transducer measurements for drainage. *Armstrong et al.* proposed two different reasons for this discrepancy; (1) short equilibration time and (2) inaccurate curvature measurement. In the following, we recalculate the curvatures for the same dataset using our new method (method 5 in Table 1), convert these to P_c values (Eq. 1, $\sigma = 0.0378$ N/m as in *Porter et al.*, 2010) and compare the outcome with the results of *Armstrong et al.* (2012a).

The improved curvature-based capillary pressure estimates show very favorable agreement with the transducer-based capillary pressures, much improved over the data of *Armstrong et al.* (2012) (**Figure 9**).

The new data set was also used to investigate the evolution of menisci curvatures for the *connected* (water) phase as saturation changed.

During imbibition, as more water enters the sample through the bottom port and oil is pushed out of the system through the top port, menisci curvatures shift towards more positive values, corresponding to lower P_c , whereas for drainage the exact opposite behavior is observed (see **supporting information, SI-1 and SI-2**). Thus, there are no surprises in terms of interpretation of the *connected* phase behavior.

3.2 Capillary pressures of disconnected phases

The accuracy gained in predicting fluid capillary pressures from curvatures facilitates the computation of liquid pressure of *disconnected* fluid components (disconnected *oil blobs*). This has not been achieved before as there has been no mechanism available for measuring the pressure state of disconnected blobs inside a three-dimensional porous medium. During main imbibition (MI), as water imbibes into the oil-filled media, blobs of oil remain that become disconnected from the bulk oil phase. **Figure 10** shows how capillary pressure and curvature evolves for the interface between disconnected oil *blobs* and connected water phase for a select number of points on the imbibition curve (the full imbibition cycle for disconnected phase is presented in **SI-3**). A number of interesting features are evident in the data. During imbibition the average pressure of the disconnected phase (calculated via interfacial curvatures) is consistently higher than the bulk connected phase (measured by transducer). Moving from left to right in **Figure 10**, as water saturation increases, more interface is established between connected water and disconnected oil (more oil is of course disconnected as we keep imbibing water into the sample). The full data set identifies data point by its number along the Main Imbibition path (MI01, MI02, and so on), however, for simplicity, only select data points are discussed here). From MI06 to MI07 a new blob is established with a curvature that is significantly different from the previous blob, corresponding to a lower capillary pressure than the previous blob, but still higher than the connected phase bulk pressure. At MI08 additional interface falls generally into two groups, one with curvature (closer to zero) corresponding to lower pressure, and a second group with smaller curvature corresponding to higher capillary pressures, and similar to the initial blob seen in MI06 (**Figure 10**, middle row).

The bottom row of images identifies the location of these various curvature values by color coding of the interfaces. Blue interfaces are associated with the peak at more negative curvatures (higher pressures), green interfaces have curvatures closer to zero. Although the average curvature keeps marching to the right, as we progress to MI09, we see that new interface is generated (as indicated by the arrows in the 3D surface plots) that has a lower curvature, i.e., a feature is added with a peak to the left of the preceding features (see red arrow in curvature histogram). As more interface is added, the average interfacial pressure of the disconnected blobs approaches the bulk tensiometer pressure. This suggests that while the pressure state of these newly developed blobs is influenced by the bulk fluid pressure, it deviates from the bulk pressure when the local pore morphology forces a different arrangement of contact lines. Larger volume disconnected blobs would be expected to have mean curvatures closer to the bulk pressure because there is greater capacity for adjusting the fluid volume to match the bulk pressure. Note that the smaller blobs in **Figure 10**, bottom row, all have curvatures that strongly deviate from the bulk pressure (noted by blue color), while the larger blob is mostly green in color indicating curvatures comparable to the bulk pressure, with small portions of the blob interface in blue. This domination of the curvature by the pore geometry forces a pressure gradient within the disconnected blob.

Figure 11 shows how capillary pressure and menisci curvature evolves for the interface between disconnected oil and connected water phase, for a select number of points on the drainage curve (the full drainage cycle for disconnected phase is presented in **SI-4**). We immediately observe that for drainage, the average pressure of disconnected phase is consistently *lower* than the connected bulk phase (and transducer-based) pressure. Keeping in mind the results for imbibition, it appears that the disconnected blobs exhibit a muted reflection of the wetting phase hysteresis; the pressure state of the disconnected phase is bounded by the pressures of the connected fluid phase (**Figure 12**). This intuitively makes sense if we consider the earlier suggestion that pressures of disconnected blobs are dominated by pore morphology, and influenced, but not entirely governed, by the pressure of the connected fluid. These results are in good agreement with the recent work of Singh et al. (2017) who analyzed in detail three representative snap-off events for a 3.8 mm diameter and 10 mm long

Ketton limestone rock sample. The authors found that “trapped phase re-arranges itself in the pore space to minimize the oil pressure” (or energy), which agrees well with our findings presented above, despite that our data concerns trapped phase across the entire sample. It should be noted here that the pressure differences between connected and disconnected phases are significant. Pressure differences in the middle of the hysteresis loop are on the order of 20-30 Pa, or about 10% of the magnitude of the connected phase pressures, which is significantly beyond the error ($< 0.02\%$) expected for image-based curvatures, see **Figure 7**.

The pressure within different disconnected phases can vary significantly. This can be seen by the sudden change in the curvature histogram between MD02 and MD05 in **Figure 11**. During drainage, as higher capillary pressures are imposed on the wetting phase, oil invades and reconnects some of the previously disconnected blobs. This reconnection of oil ganglia was also observed by Andrew et al. (2015). In this sequence of images, the rather large multi-pore ganglion of disconnected nonwetting phase that exists through MD02 (see red arrow in surface plot) is not sustained at higher wetting-phase capillary pressures as we progress to MD05 (intermediate points between MD02 and MD05 did not capture any changes in the fluid configurations and are therefore omitted). As a result of this substantial change in fluid configuration, the curvature histogram for MD05 displays a corresponding rather large shift to the left, i.e., to higher average curvature and thus lower disconnected phase P_c values. By removing the large ganglion, the interfacial P_c is now dominated by the remaining disconnected blobs. Their contribution could always be seen in the histogram as a smaller peak to the left of the main peak, but it is the removal of the large ganglion that clarifies the identification of the contribution by these smaller disconnected blobs.

Discussion

X-ray tomography-based imaging is the only tool presently available for non-invasively exploring multiphase dynamics within porous media at the resolution needed to study interfaces and disconnected blobs. In the past, when quantifying the pressure-saturation relationship, the study was limited to the pressure distribution of *connected* phases that could be verified by tensiometers. The new algorithm for estimating curvatures that is presented

herein has permitted for the first time sufficient confidence to investigate the capillary pressure dynamics of *disconnected* phases during drainage and imbibition. In doing so, it became evident that the pore architecture plays a strong role in the capillary pressure of disconnected phases. The discrepancy between bulk (connected phase) pressure and capillary pressure of trapped blobs is especially notable for the smaller blobs. It is suggested here that for a trapped blob to equilibrate to the bulk pressure requires a sufficient minimum volume and overcoming contact angle hysteresis. The concept of a sufficient minimum volume is interesting. Small blob volume will constrain the options for location of its interfaces. The resulting capillary pressure will be determined by an energetic competition between the pore radii, the contact angle, and contact line adherence (**Figure 13**). Contact line adherence and its associated contact angle hysteresis can impose pressure gradients across a blob, as seen by the variation in color for different interfaces of the same blob in **Figures 10 and 11**), and illustrated in greater detail in **Figure 14** for two select interfaces (one for imbibition and one for drainage). Insight on the surface properties of the porous medium could be gained by investigating the width of the distribution of curvatures (the second moment) associated with disconnected blobs. It is expected that the impact of pore geometry would be less for larger disconnected blobs, where the volume can explore more pore space. This might be the case for the glass bead data presented by *Garing et al.* (2017). Their data analysis included only a single saturation point where the disconnected phase consisted of a fairly large ganglion. We hypothesize that disconnected phase for lower saturations, where the ganglia become smaller, is more affected by the surrounding pore geometry, and therefore each ganglia may consist of a wider distribution of curvatures as we see in this study. Also, we expect that the resulting non-wetting configuration from water flowing down a rock and trapping air would be very different than that resulting from water and oil that is pumped under pressure back and forth as we do in our experiments. In the case of Garing et al., capillary pressures are quite close to the air entry pressures and completely controlled by pore size. In their brine gravity filling there is little potential for development of contact angle hysteresis. As brine moves into the system, the wetting interface will move into the air-filled pores until the pressure of the air-phase is sufficient to stop the interface advance. By contrast, in our system, as isolated blobs try to equilibrate to changes in pressure, hysteresis

effects may come into play as curvature and contact lines try to adjust. For larger blobs that expand into many pores, the pressure gradients across the blob and the second moment of the distribution of curvatures could be used to investigate the degree of hysteresis that is associated with solid-surface properties, providing valuable analytical tools as this technique is applied to real porous media.

Conclusions

This work presents novel measurements of the internal pressure of a *disconnected* oil blob. This was facilitated by a new method we developed for estimating, from CMT images, the curvature of liquid-liquid interfaces within porous media. The new method raises the accuracy overall from 91.4 to 94.5%, and for pores with radii in excess of 50 voxels, the accuracy is increased to 99.8%. Since to date, quantifying pressure-saturation relationships for multiphase fluids in porous media was limited to measuring the *connected* fluid phase with tensiometers, this new tool significantly expands the potential for understanding the physics of multiphase flow. The improvement was achieved by reducing the contribution associated with the interfacial zone near the contact line, where liquid-solid phase interactions and image inaccuracies add artifacts to the data. The new curvature estimation method included the elimination of data within a distance threshold of the solid surface (surface modification) and a distance weighting approach. It should be noted that this study was conducted on CMT data that is 10 years old with a voxel resolution of 13 microns. With the improvements in the CMT technique, we now regularly collect CMT data at 2-4 micron resolution, and would expect even better performance of the curvature estimation algorithm.

However, there are of course also limitations to the approach, and we expect that as the porous medium becomes increasingly complex, and pore sizes approach the limit of image resolution, it becomes more difficult to estimate the curvatures with this level of accuracy. It is worth mentioning that Singh et al. (2017) define the (Euclidean) dilation distance in three dimensions normal to the solid surface, whereas we define our non-Euclidean contact line distance on a curved surface. The triangle can be more than 10 units away from the contact line, but still be within the much shorter dilation distance from the solid surface, especially on

water-wet surface with acute contact angles. Thus, we hypothesize that the approach presented here could potentially be more flexible or robust, especially at relatively coarse resolution where a three-dimensional dilation by 2-3 voxels would eliminate a large part of the “good” triangles. In favor of this hypothesis, Herring et al. (2017) presented very convincing data for multi-phase flow in a Bentheimer sandstone using an algorithm similar to ours.

Using this method, we explored the pressure state of *disconnected* nonwetting phase during drainage and imbibition. We made a number of unprecedented observations that sheds light on the fundamentals of multi-phase flow in porous media. First, during wetting phase drainage, multi-pore ganglia of disconnected nonwetting phase are not sustained; as saturation decreases, they reconnect to the main non-wetting phase. During wetting phase imbibition, the pressure state of individual blobs appears to be more strongly controlled by pore morphology than by bulk fluid pressure (blobs are established at pressures above the bulk fluid pressure, out of sequence). The pressure-saturation curve for the disconnected (non-wetting) phase forms a hysteretic envelope that exists well inside of the main hysteresis loop of the connected wetting phase.

This new and significantly more accurate method for estimating interfacial curvature in CMT images provides a novel tool to advance investigations of multiphase flow in porous media by permitting the accurate analysis of connected and disconnected phases.

Acknowledgements

This research was supported by the US National Science Foundation, award #1344877. This research used resources of the Advanced Photon Source, a U.S. Department of Energy (DOE) Office of Science User Facility operated for the DOE Office of Science by Argonne National Laboratory under Contract No. DE-AC02-06CH11357. We acknowledge the support of GeoSoilEnviroCARS (Sector 13), which is supported by the National Science Foundation - Earth Sciences (EAR-1128799), and the Department of Energy, Geosciences (DE-FG02-94ER14466). We thank Mark Rivers at the Advanced Photon Source for assistance at the GSECARS beam line.

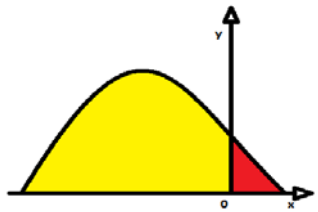
References

- Andrew, M., Bijeljic, B. and Blunt, M.J. (2014). Pore-by-pore capillary pressure measurements using X-ray microtomography at reservoir conditions: Curvature, snap-off, and remobilization of residual CO₂. *Water Resources Research*, 50, 8760-8774.
- Andrew, M., Bijeljic, B. and Blunt, M. (2015) Reservoir Condition Pore-scale Imaging of Multiple Fluid Phases Using X-ray Microtomography. *Transport in Porous Media* (96), e52440.
- Armstrong, R.T., Georgiadis, A., Ott, H., Klemin, D. and Berg, S. (2014). Critical capillary number: Desaturation studied with fast X-ray computed microtomography. *Geophysical Research Letters*, 41(1), 55-60.
- Armstrong, R.T., Porter, M.L. and Wildenschild, D. (2012a). Linking pore-scale interfacial curvature to column-scale capillary pressure. *Advances in Water Resources*, 46, 55-62.
- Armstrong, R.T., Pentland, C.H., Berg, S., Hummel, J., Lichau, D. and Bernard, L. (2012b). Estimation of Curvature From Micro-CT Liquid-Liquid Displacement Studies with Pore Scale Resolution, *International Symposium of the Society of Core Analysts* held in Aberdeen, Scotland, UK, 27-30 August 2012, At Aberdeen, Scotland, UK, Volume: SCA2012-55
- Armstrong, R.T. and Wildenschild, D. (2012) Investigating the pore-scale mechanisms of microbial enhanced oil recovery. *Journal of Petroleum Science and Engineering* 94-95, 155-164.
- Bullard, J.W., Garboczi, E.J., Carter, W.C. and Fuller Jr, E.R. (1995). Numerical methods for computing interfacial mean curvature. *Computational Materials Science*, 4(2), 103-116.
- Cheng, J.T., Pyrak-Nolte, L.J., Nolte, D.D. and Giordano, N.J. (2004). Linking pressure and saturation through interfacial areas in porous media. *Geophysical Research Letters*, 31(8), L08502 08501-08504.
- Dijkstra, E. (1959). A Note on Two Problems in Connexion with Graphs. *Numerische Mathematik*, 3.
- Garinga, C., J.A. de Chalendar, M. Voltolini, J.B. Ajo-Franklin, S.M. Benson, (2017) Pore-scale capillary pressure analysis using multi-scale X-ray micromotography. *Adv. in Water Resources*, 104, 223–241, <https://doi.org/10.1016/j.advwatres.2017.04.006>.
- Gray, W. G., A. L. Dye, J. E. McClure, L. J. Pyrak-Nolte, and C. T. Miller (2015), On the dynamics and kinematics of two-fluid-phase flow in porous media, *Water Resources Research*, 51 (7), 5365–5381, doi:10.1002/2015WR01692.
- Garing, C., J.A. de Chalendar, M. Voltolini, J.B. Ajo-Franklin, S.M. Benson (2017). Pore-scale capillary pressure analysis using multi-scale X-ray micromotography, *Advances in Water Resources* 104
- Herring, A.L., Middleton, J., Walsh, R., Kingston, A. and Sheppard, A. (2017) Flow rate impacts on capillary pressure and interface curvature of connected and disconnected fluid phases during multiphase flow in sandstone. *Advances in Water Resources* 107(Supplement C), 460-469. (2017) 223–241, <http://dx.doi.org/10.1016/j.advwatres.2017.04.006>
- Li, Tianyi, MS thesis, Oregon State University, <https://ir.library.oregonstate.edu/downloads/rv042w87m>
- Lorensen, W.E. and Cline, H.E. (1987). Marching Cubes: A high resolution 3D surface construction algorithm. *Computer Graphics*, (ACM) 21(4), 163-169.
- Porter, M. and Wildenschild, D. (2010). Image analysis algorithms for estimating porous media multiphase flow variables from computed microtomography data: a validation study. *Computational Geosciences*, 14(1), 15-30.
- Porter, M.L., Wildenschild, D., Grant, G. and Gerhard, J.I. (2010). Measurement and prediction of the relationship between capillary pressure, saturation, and interfacial area in a NAPL-water-glass bead system. *Water Resources Research*, 46(8).

- Rivers, M.L., Sutton, S.R. and Eng, P. (1999). Geoscience applications of x-ray computed microtomography. *Proceedings of SPIE - The International Society for Optical Engineering*, 3772, 78-86.
- Schlüter, S., A. Sheppard, K. Brown, and D. Wildenschild (2014). Image processing of multiphase images obtained via x-ray microtomography: A review, *Water Resour. Res.*, 50, doi:10.1002/2014WR015256.
- Schlüter, S., S. Berg, T. Li, H-J. Vogel, and D. Wildenschild (2017). Time scales of relaxation dynamics during transient conditions in two-phase flow, accepted, *Water Resources Research*. Singh, K., B. Bijeljic, and M. J. Blunt (2016), Imaging of oil layers, curvature and contact angle in a mixed-wet and a water-wet carbonate rock, *Water Resour. Res.*, 52, 1716–1728, doi:10.1002/2015WR018072.
- Singh, K., Menke, H., Andrew, M., Lin, Q., Rau, C., Blunt, M.J. and Bijeljic, B. (2017) Dynamics of snap-off and pore-filling events during two-phase fluid flow in permeable media. *Scientific Reports* 7(1), 5192.
- Thirion, J.-P. and Gourdon, A. (1995). Computing the differential characteristics of isointensity surfaces. *Computer Vision and Image Understanding*, 61(2), 190-202.

TABLES

Table 1. Mean curvature estimation methods.

Approaches:	Details:	Formula:
1. Original	Mean curvature calculated based on the original histogram.	$K_m = (K_1 + K_2)/2$
2. Negative values only	Mean curvature calculated based on all the negative values in the original histogram (yellow area under the curve) as in Armstrong et al. (2012a)	$K_m = \frac{K_1 + K_2}{2} \text{ for } K < 0$ 
3. Distance weighting only	Curvature weighted as a function of distance values for each triangle.	$K_{m,dw} = \frac{\sum_i^N K_i D_i}{\sum_i^N D_i}$
4. Surface modification only	Mean curvature calculated based on the remaining interface; removal of triangles closer than a set threshold.	$K_{m,sm} = (K_1 + K_2)/2 \text{ for } D_i > D_{min}$
5. Distance weighting combined with surface modification	Curvature weighted as a function of distance values for each triangle for the remaining interface (after removal of triangles below threshold value).	$K_{m,dw+sm} = \frac{\sum_i^N k_i D_i}{\sum_i^N D_i} \text{ for } D_i > D_{min}$

FIGURES

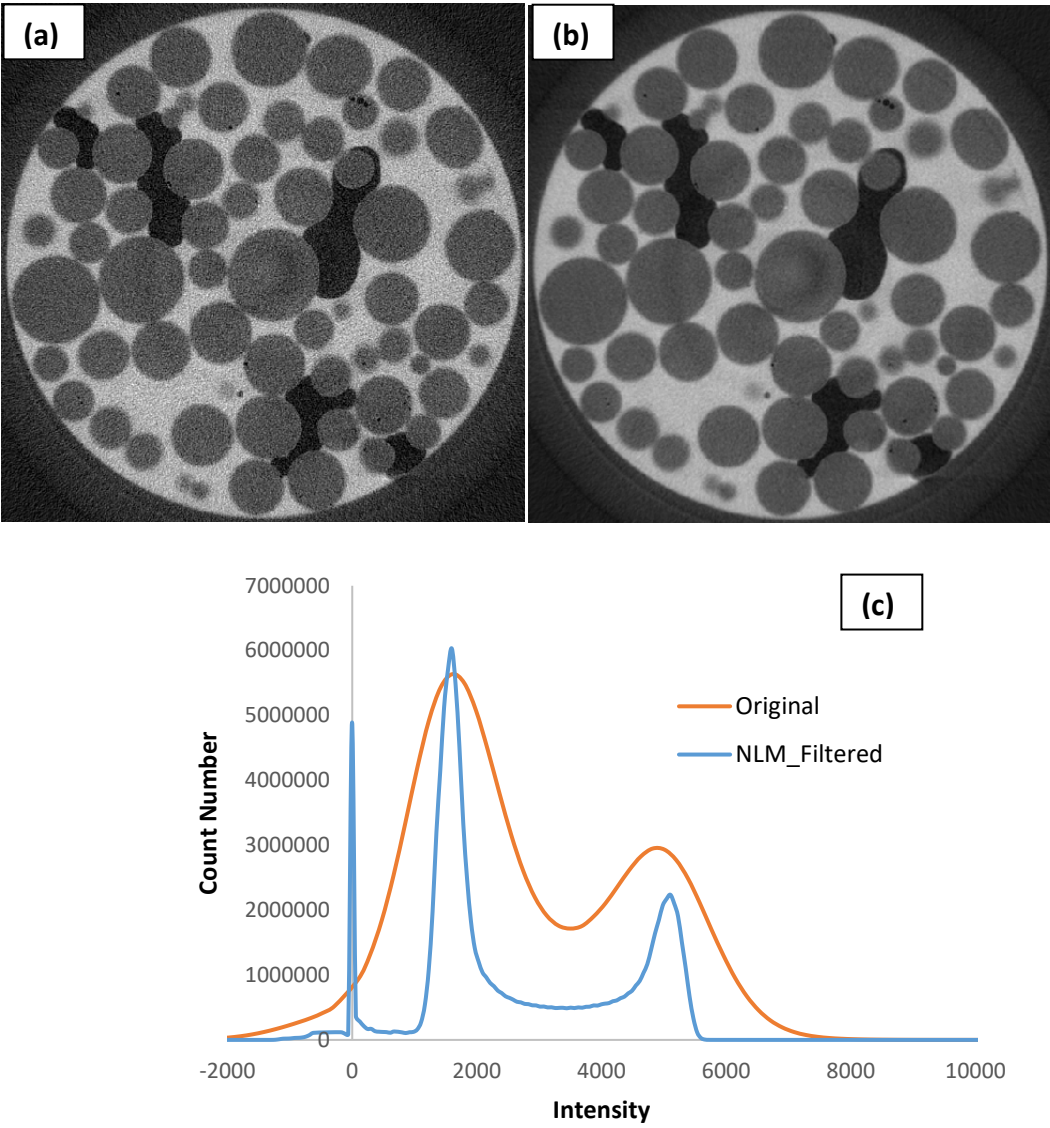


Figure 1. Example images of the original greyscale **(a)** and non-local means filtered **(b)** and corresponding intensity histograms **(c)**. The three distinct peaks emerging after NLM filtering represent, from left to right, oil, beads, and water (KI-solution).

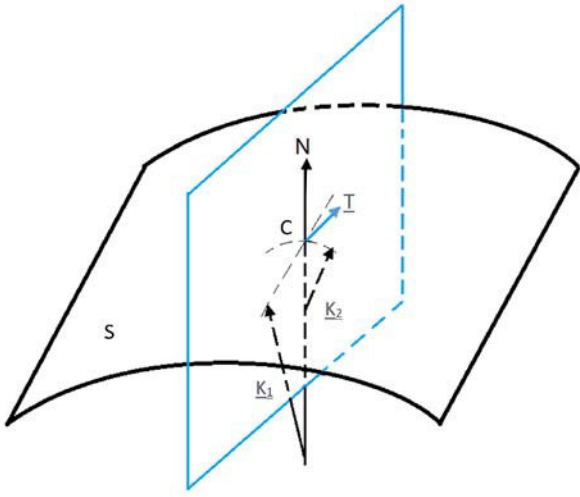


Figure 2. Small segment of an interface S. Curvature is measured at point C. As the plane is rotated about the normal, N, a tangent vector, T, is formed and a curvature is defined via the two principal curvatures, K_1 and K_2 .

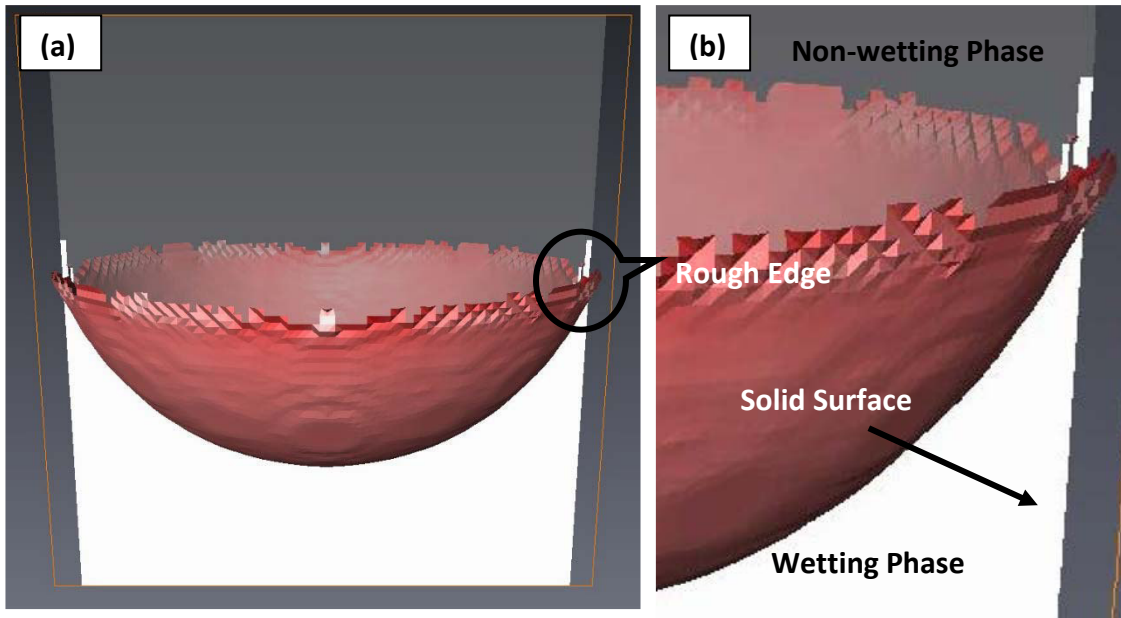


Figure 3. (a) surface rendering of the synthetic capillary tube fluid-fluid interface (red) between non-wetting (grey) and wetting phase (white) in a synthetically generated capillary tube ($r = 50$ voxels), and (b) illustration of the rough edge that exists close to the solid surface. Note that any grey-scale image (i.e., a discretized surface), regardless of resolution, is a pixelated version of reality and as such application of a threshold will result in a somewhat rough contact-line.

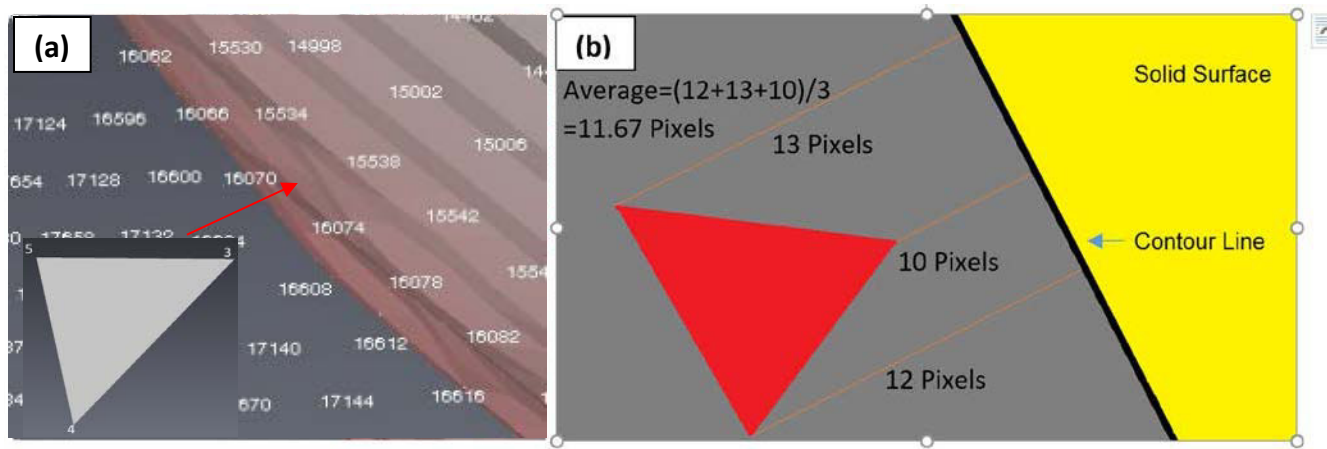


Figure 4. (a) triangulated interface with vertex view, and (b) shortest edge distance calculation.

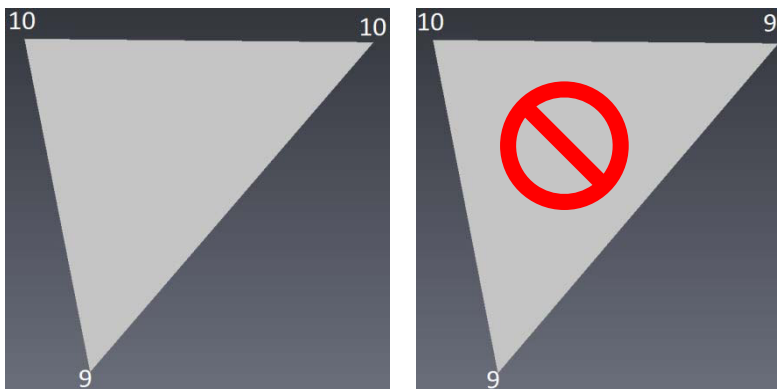


Figure 5. Single triangle showing vertex shortest distance values. The triangle on the left has an average distance of $(10 + 10 + 9) / 3 = 9.67$, which is above a chosen threshold of 9.5. The triangle on the right is eliminated as the distance to the solid surface $(10 + 9 + 9) / 3 = 9.33$ is shorter than the chosen threshold.

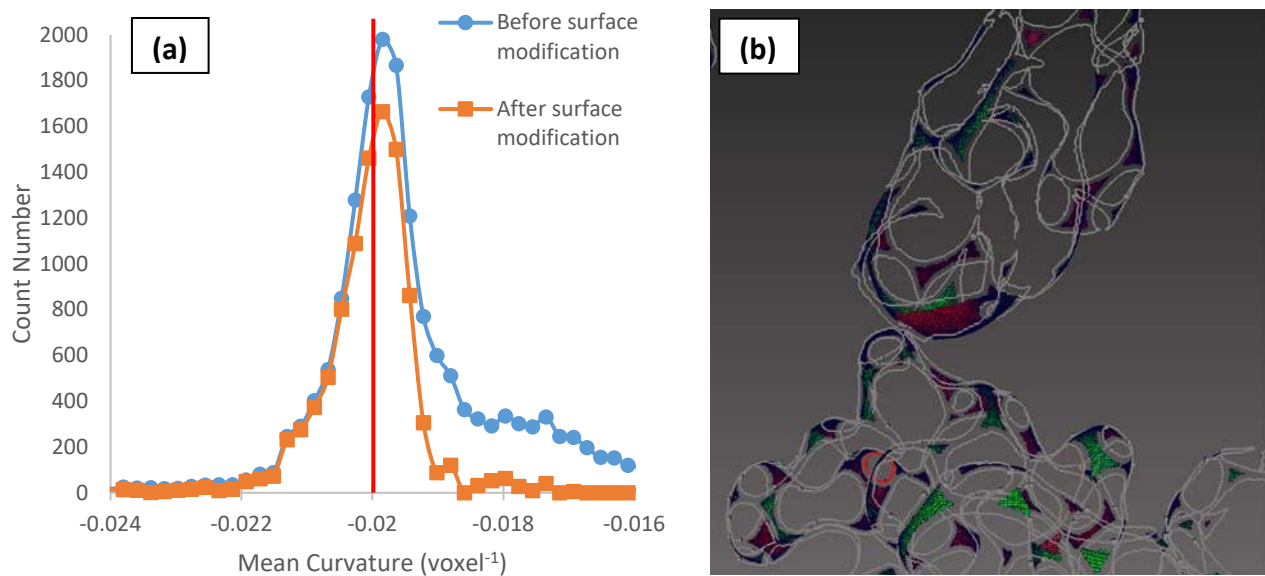


Figure 6. (a) Mean curvature histogram for synthetic capillary tube with 50 voxel radius before and after the surface has been modified to eliminate effects of the solid surface. The red vertical line represents the theoretical curvature. **(b)** Example surface modification resulting from clipping the triangles near the solid surface using an edge distance threshold (D_{\min}) of 20%.

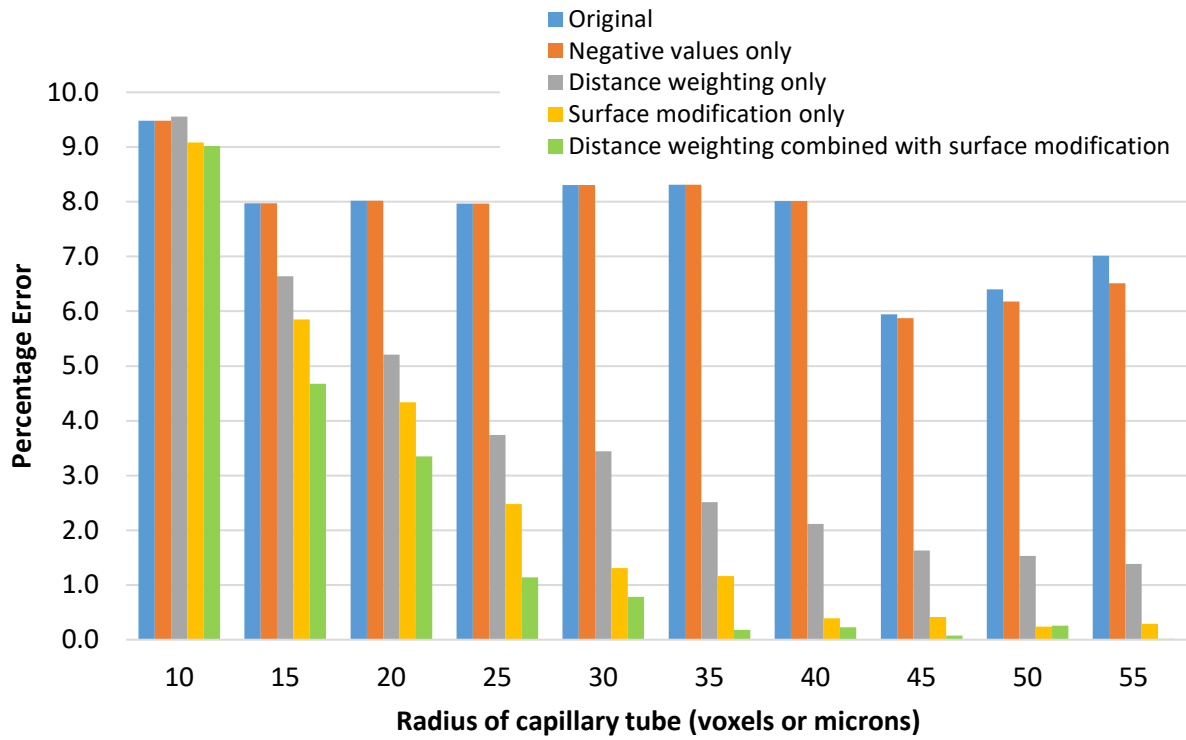


Figure 7. Percentage error of mean curvature estimates, corresponding to each curvature estimation method.

Method	Slope
1. Original	0.914
2. Negative values only	0.9142
3. Distance weighting only	0.9314
4. Surface modification only	0.9397
5. Distance weighting combined with surface modification	0.9451

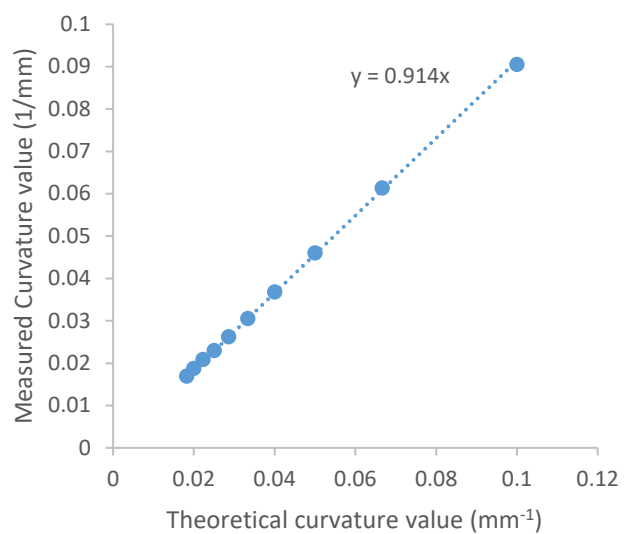


Figure 8. Table showing the slope of the linear fit for each of the five approaches. Plot of theoretical vs. measured curvatures for the first approach (Original) and the resulting linear fit.

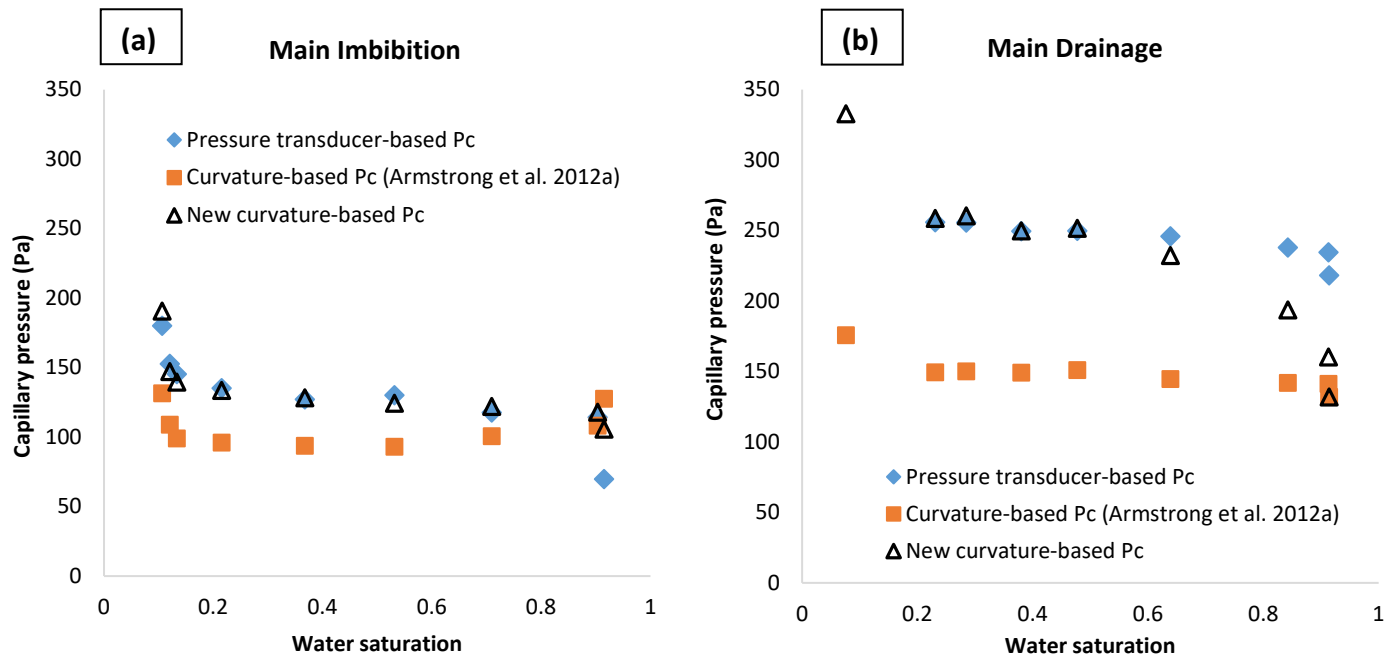


Figure 9. Comparison of P_c - S relationship obtained from transducer data and image-based curvature estimates for connected fluid-fluid interfaces: main imbibition **(a)** and main drainage **(b)**.

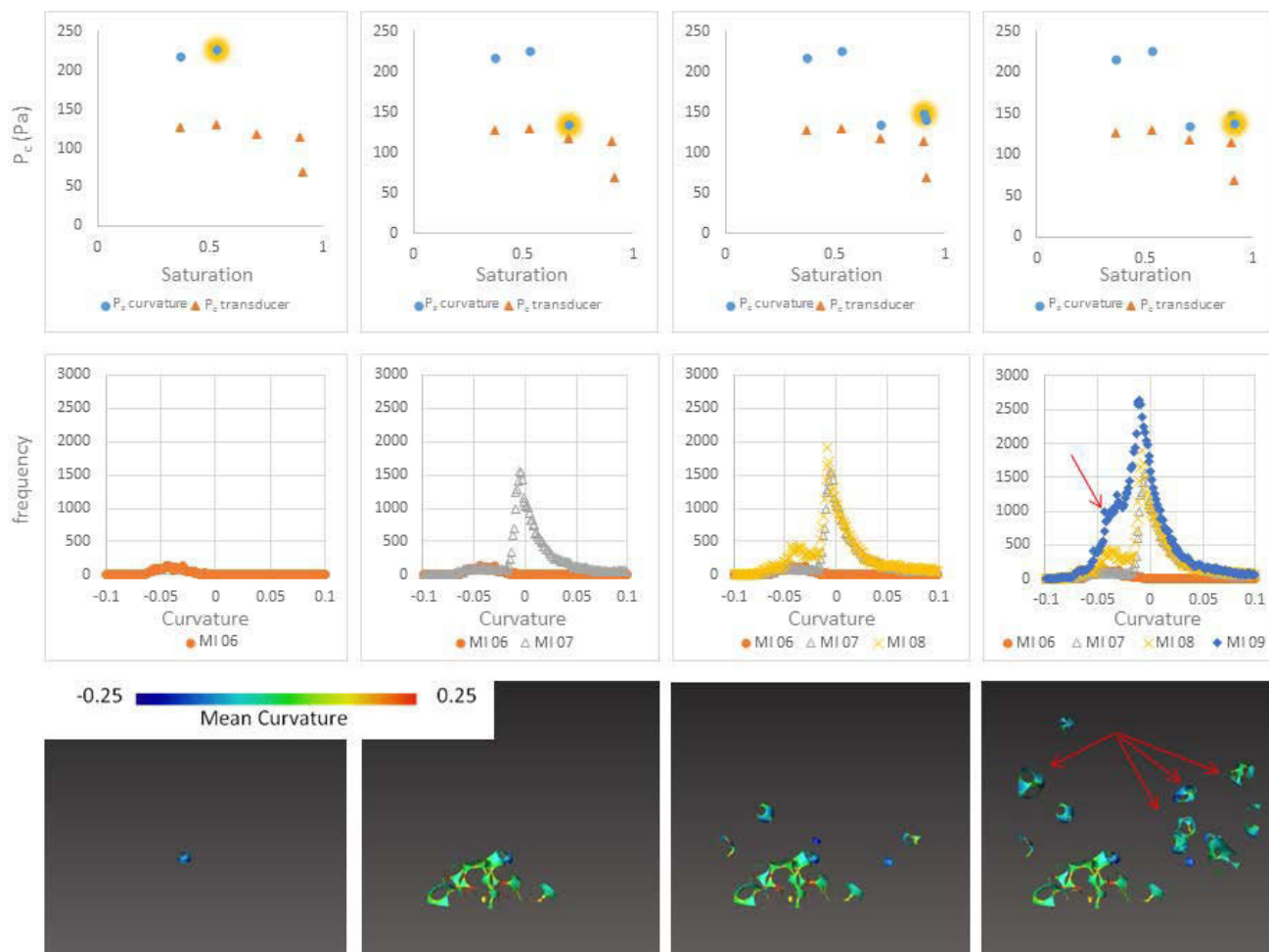


Figure 10. Sequence of images depicting the evolution of interfacial curvature (voxel⁻¹) during **imbibition** (left to right) of the wetting phase for interfaces between disconnected oil and connected water. The top row shows the P_c - S curves for transducer-based and curvature-based capillary pressures. The middle row illustrates how the curvature distributions evolve during imbibition (each histogram represents the distribution of curvatures at each saturation point), and the bottom row shows 3D surface visualizations of the evolving interfaces, color-coded according to their mean curvature values. The yellow highlights around the data points in the top (P_c - S) plots indicate the saturation state of the middle and bottom row illustrations.

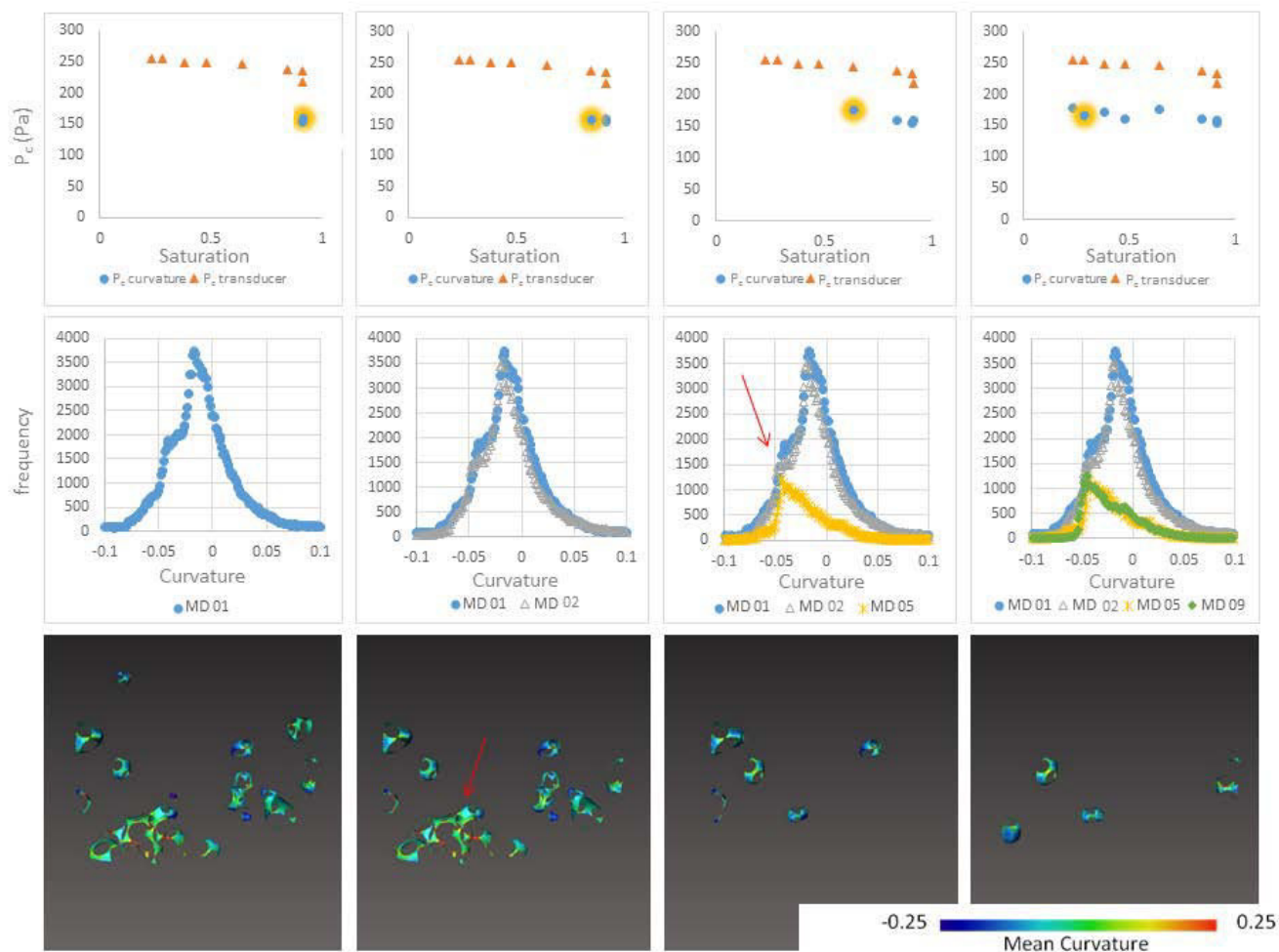


Figure 11. Sequence of images depicting the evolution of interfacial curvature (voxel⁻¹) during **drainage** (left to right) of the wetting phase for interfaces between disconnected oil and connected water. The top row shows the P_c -S curves for transducer-based and curvature-based capillary pressures. The middle row illustrates how the curvature distributions evolve during imbibition (each histogram represents the distribution of curvatures at each saturation point), and the bottom row shows 3D surface visualizations of the evolving interfaces, color-coded according to their mean curvature values. The yellow highlights around the data points in the top (P_c -S) plots indicate the saturation state of the middle and bottom row illustrations.

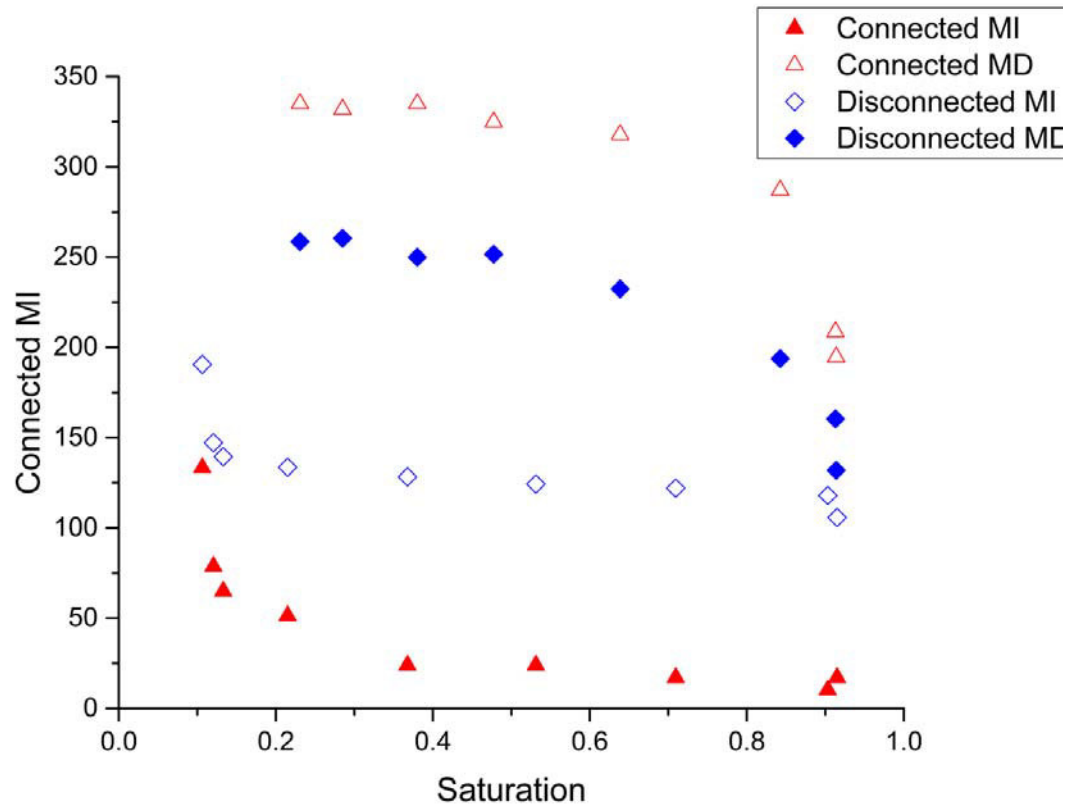


Figure 12. Comparison of P_c - S relationship for connected and disconnected fluids for main imbibition (MI) and main drainage (MD). All data points represent image-based curvature estimates (average of all blobs at each saturation). No data points are available for the disconnected phase at low wetting-phase saturations, since disconnected blobs have not formed yet.

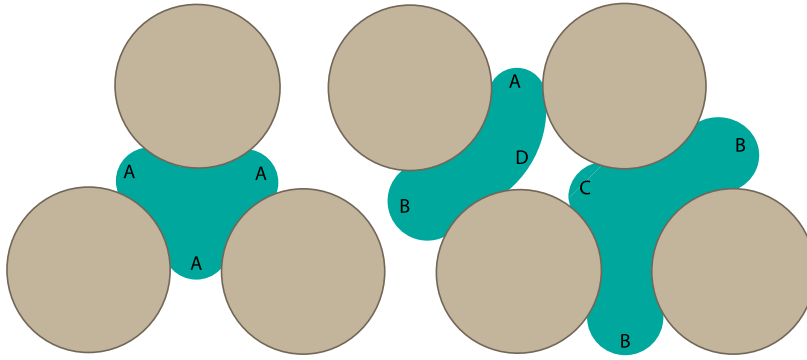


Figure 13. The figure demonstrates different potential configurations for a disconnected blob depending on whether the blob is required to have the same curvature at all interfaces, or same contact angle at all triple lines. Left blob exhibits the same contact angle and curvature at all interfaces and thereby there are no pressure gradients across the blob. The middle and right blobs exhibit the same contact angle at all triple points but not the same curvatures, generating pressure gradients across the blob. Green is oil, clear is water, brown are glass beads. Curvatures in the sketch, normalized to the radius of the beads: A, B, C and D are 2.4, 2.3, 1.8 and 0.3, respectively.

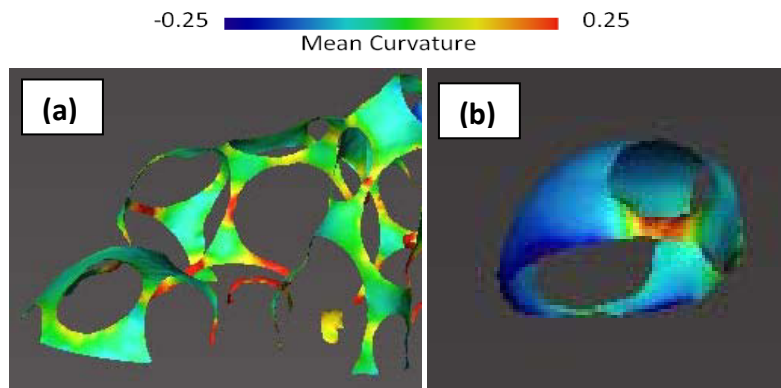
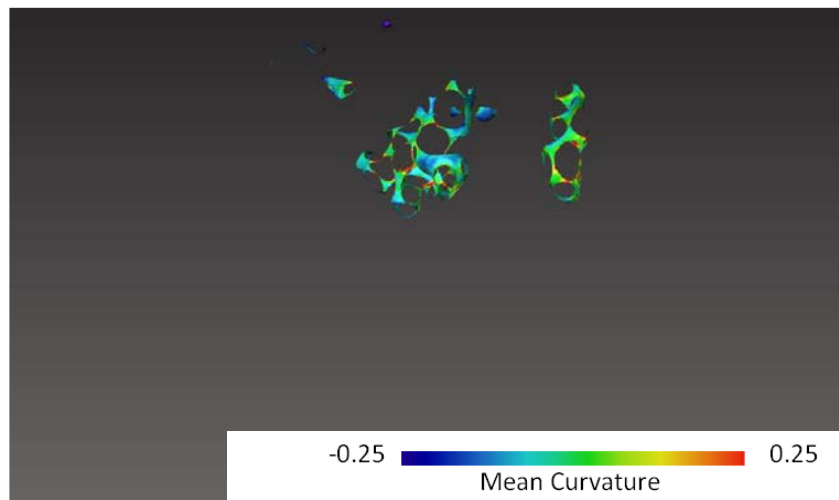
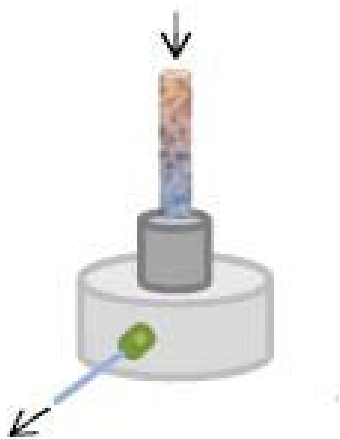


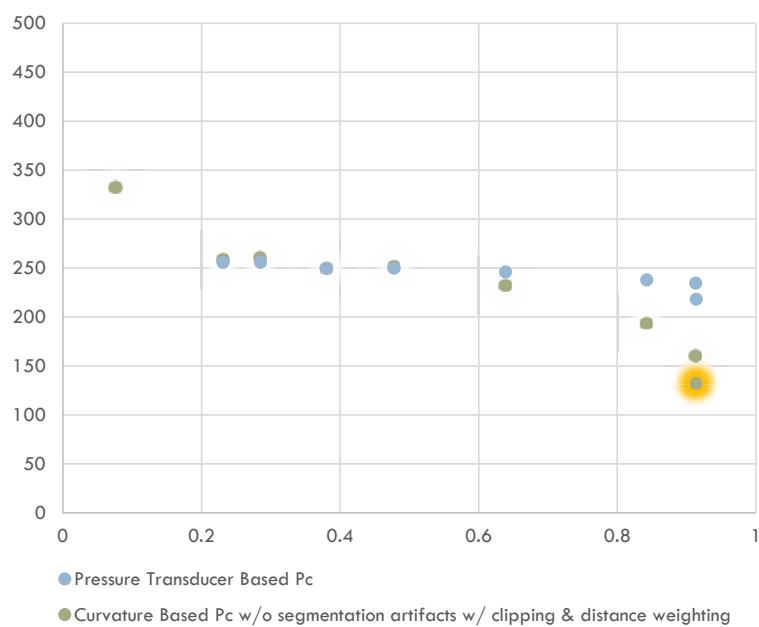
Figure 14. Enlarged images showing significant variation in interfacial curvature values (voxel^{-1}), as indicated by the color spectrum, across two different disconnected blobs, suggesting pressure gradients exist across each blob. **(a)** Main imbibition step 7, **(b)** Main drainage step 1.

MAIN DRAINAGE

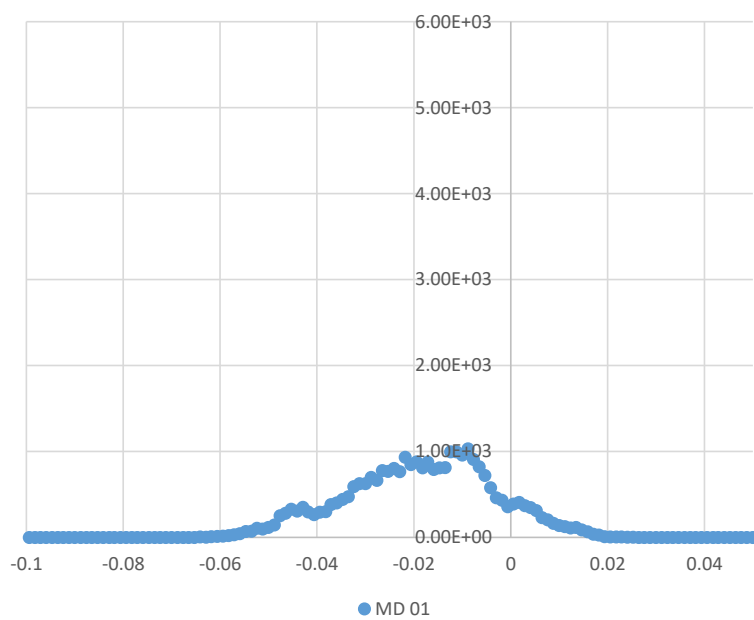
Connected phases

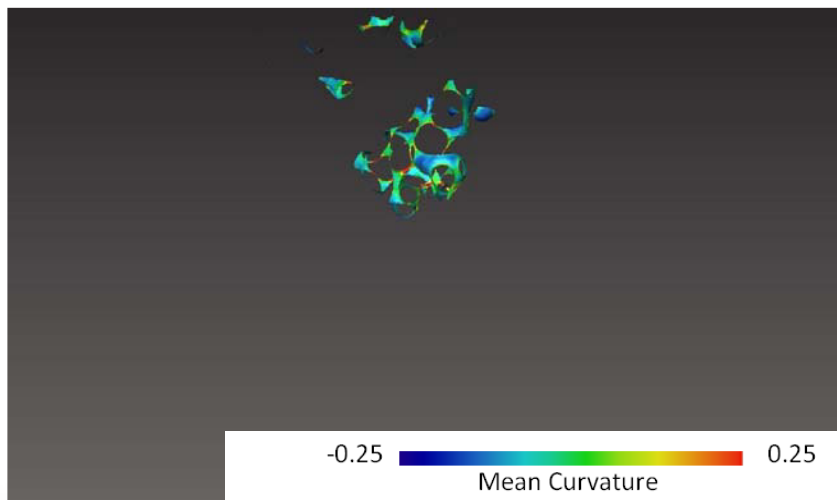
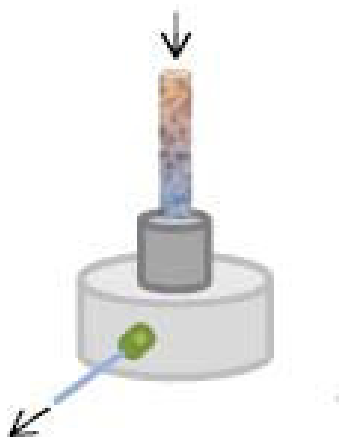


Main Drainage

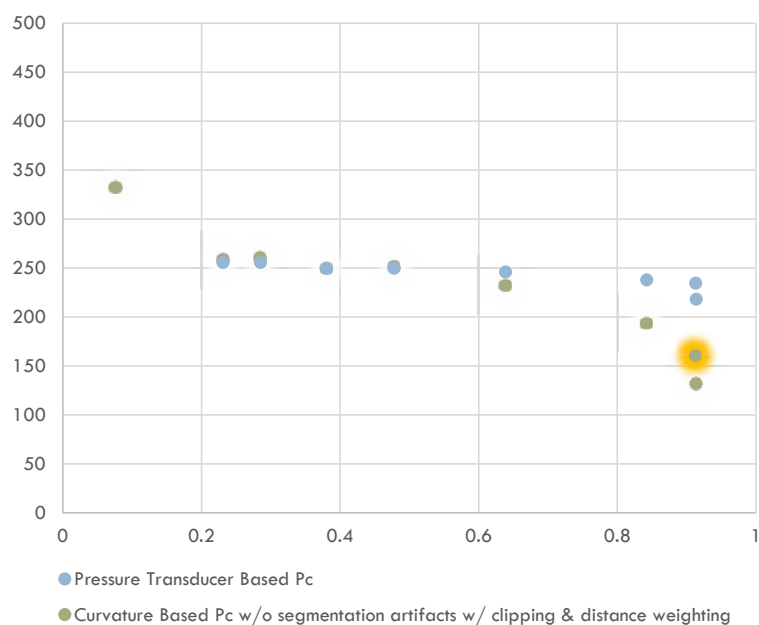


Mean Curvature Histogram

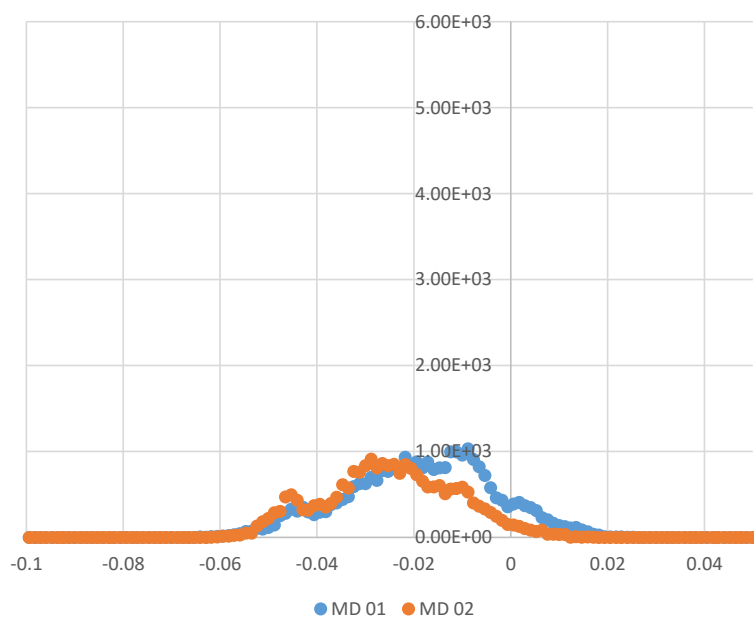


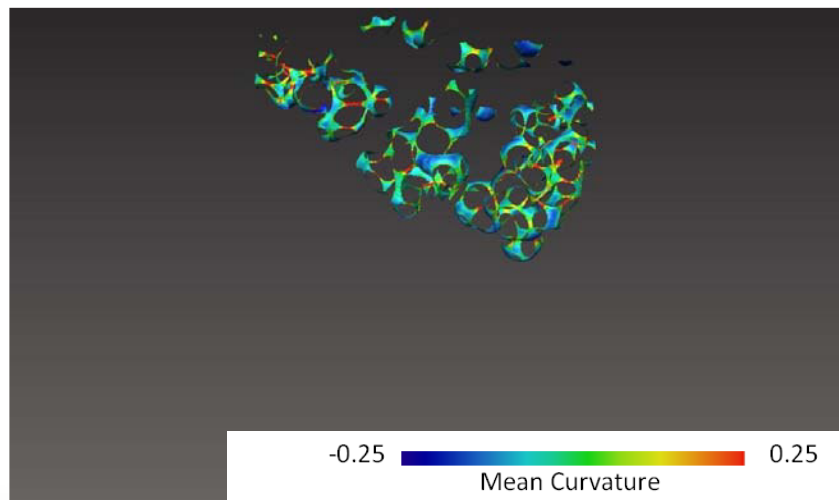
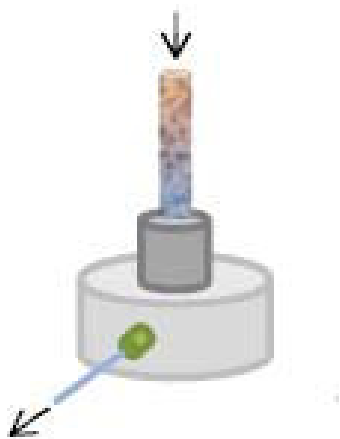


Main Drainage

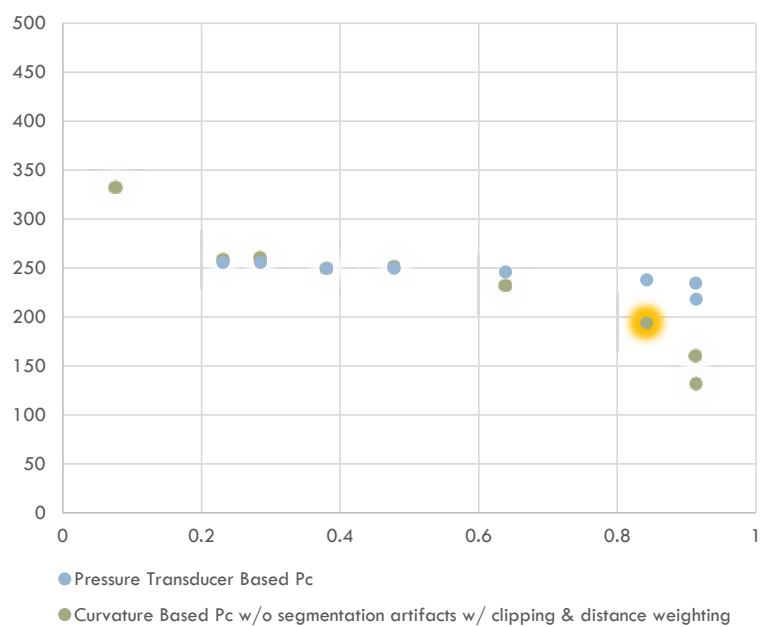


Mean Curvature Histogram

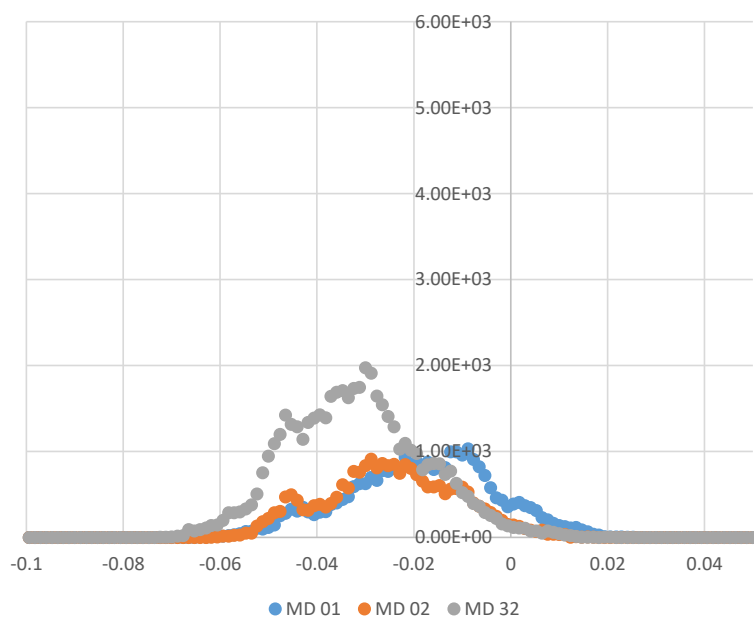


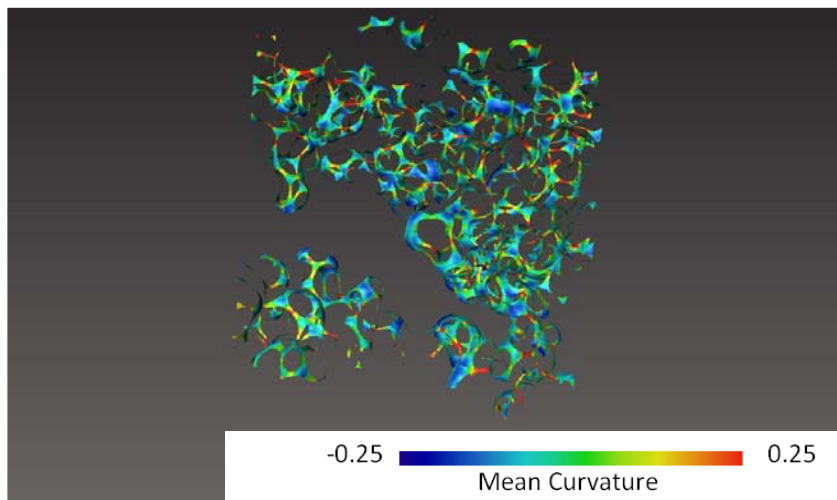
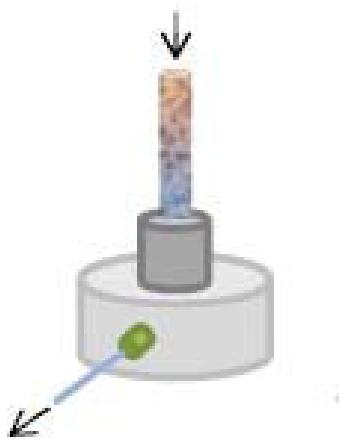


Main Drainage

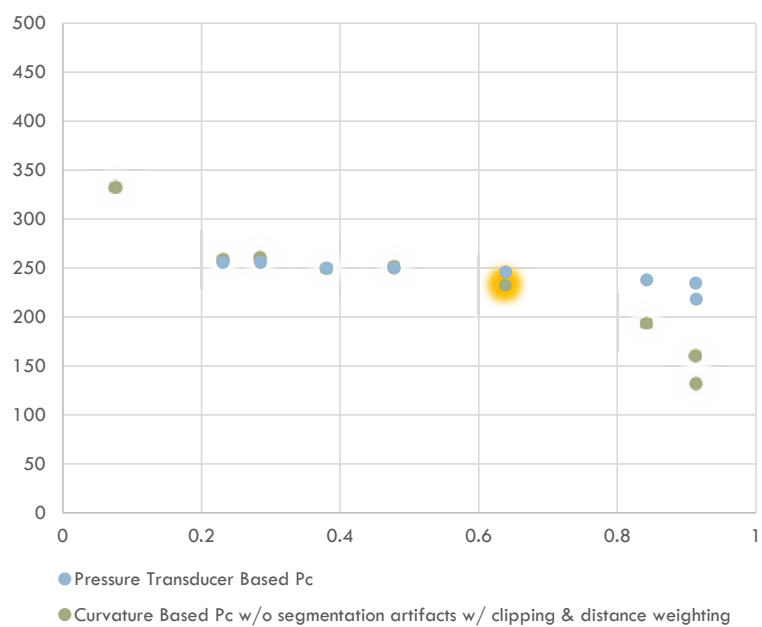


Mean Curvature Histogram

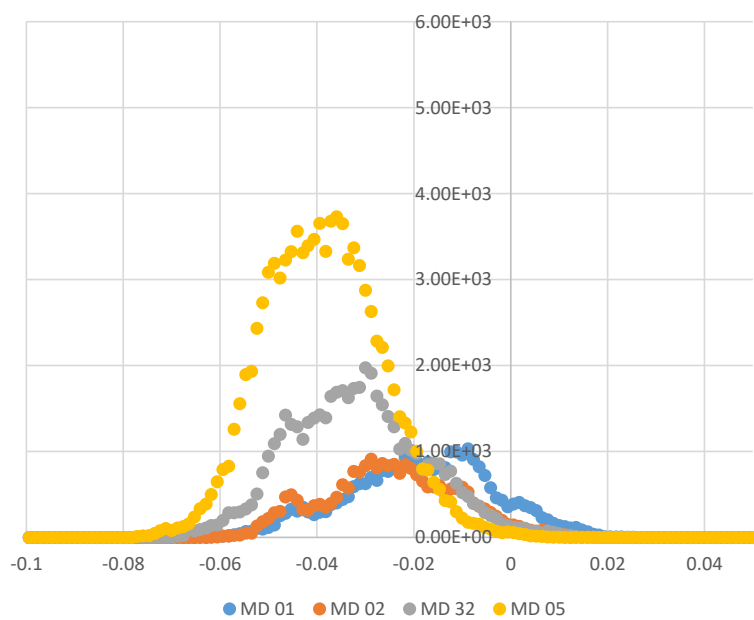


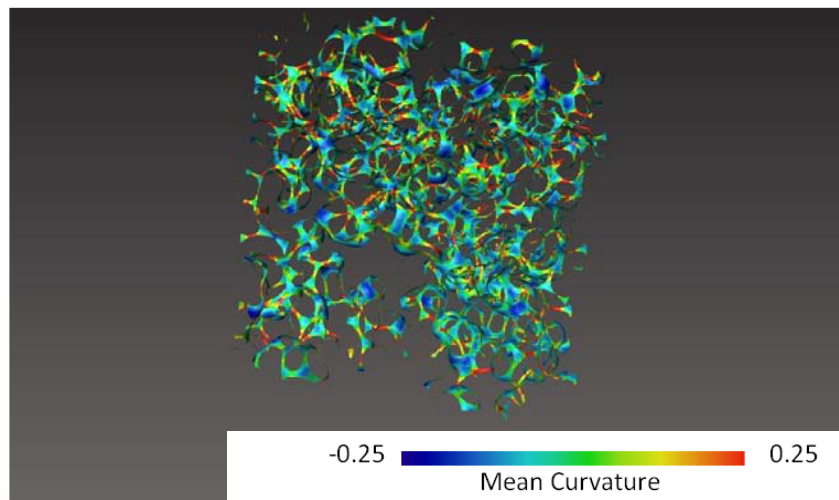
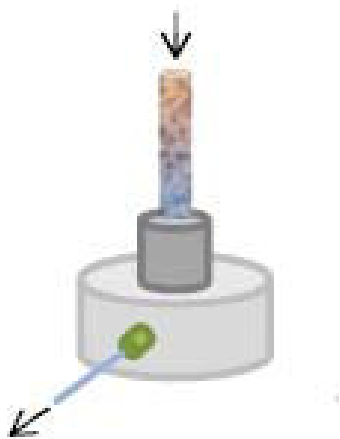


Main Drainage

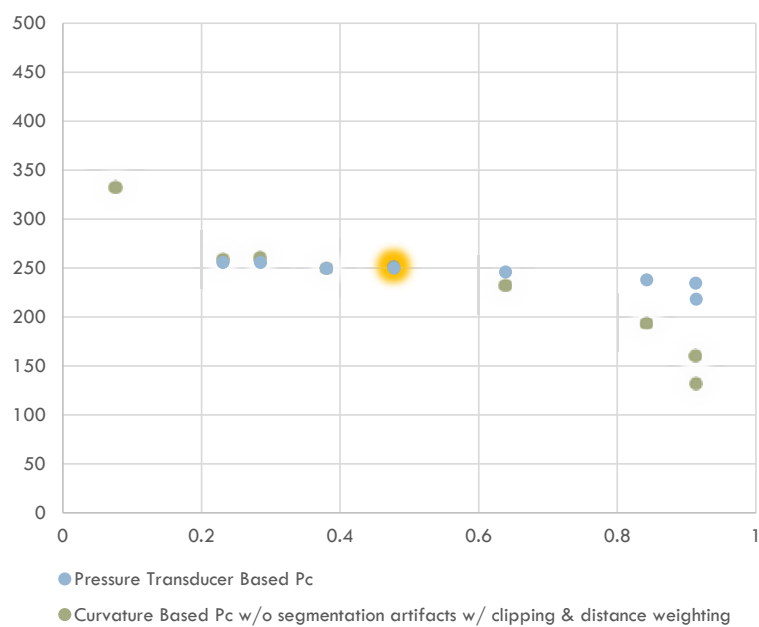


Mean Curvature Histogram

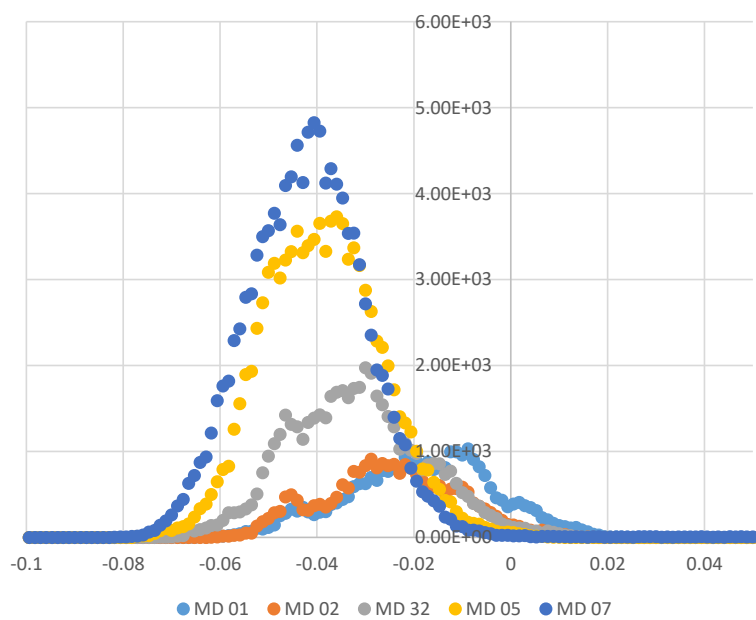


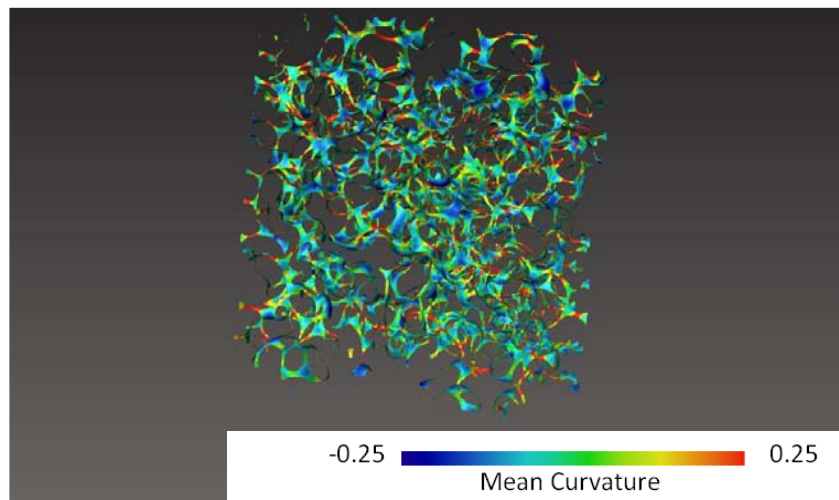
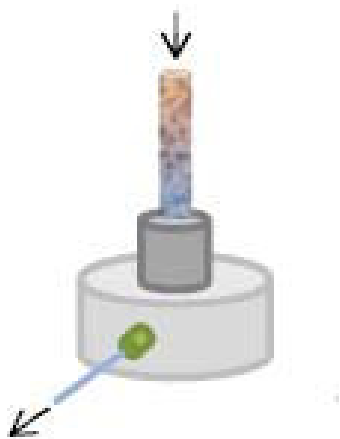


Main Drainage

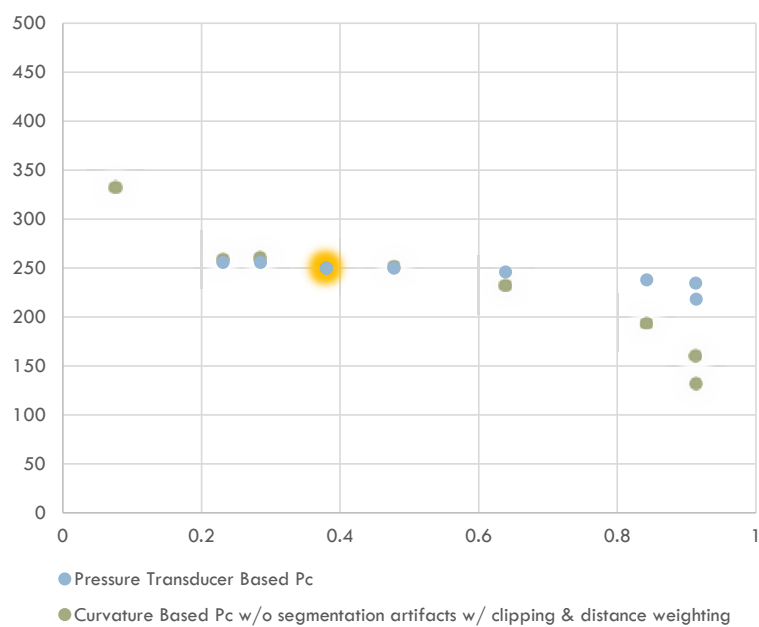


Mean Curvature Histogram

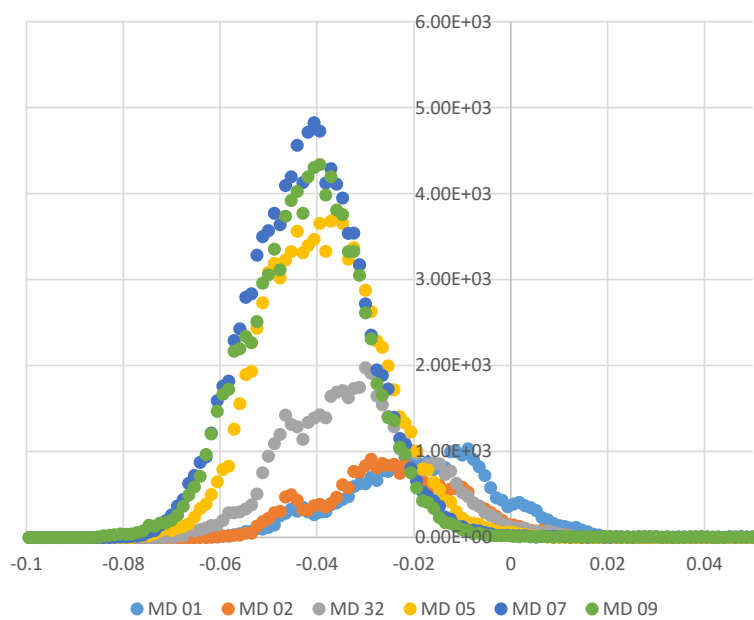


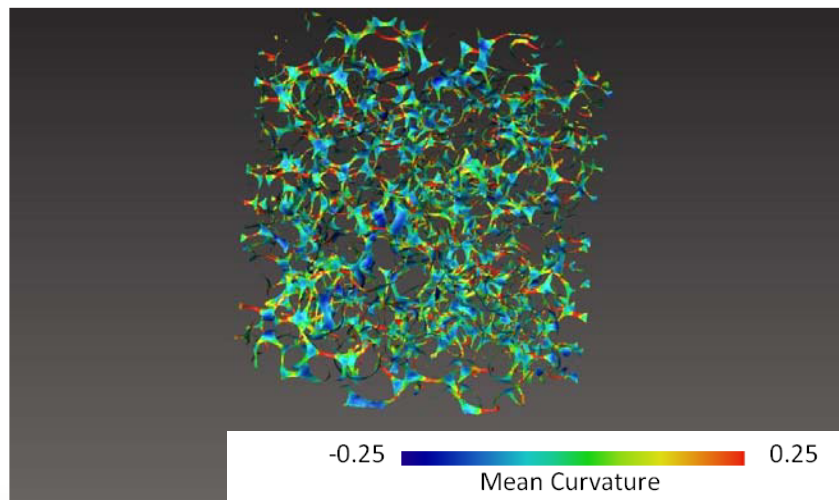
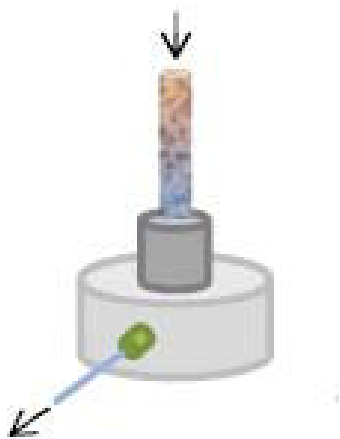


Main Drainage

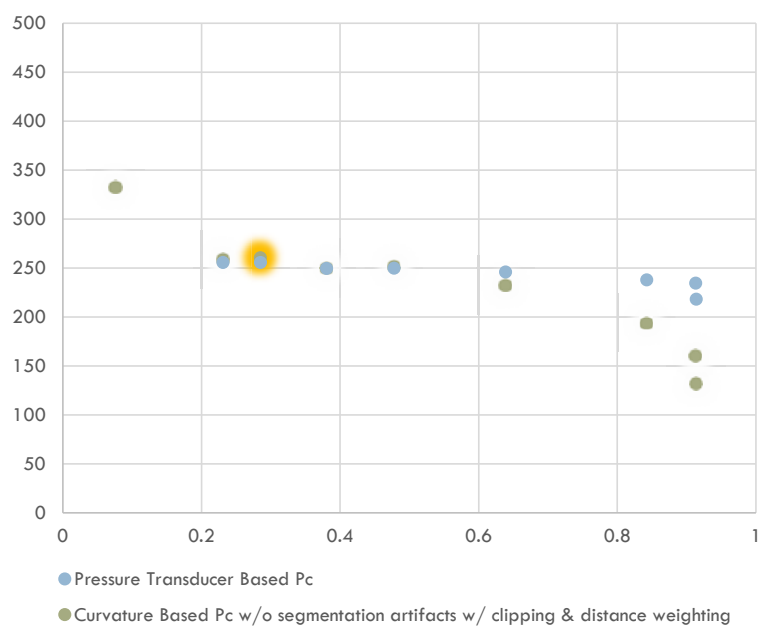


Mean Curvature Histogram

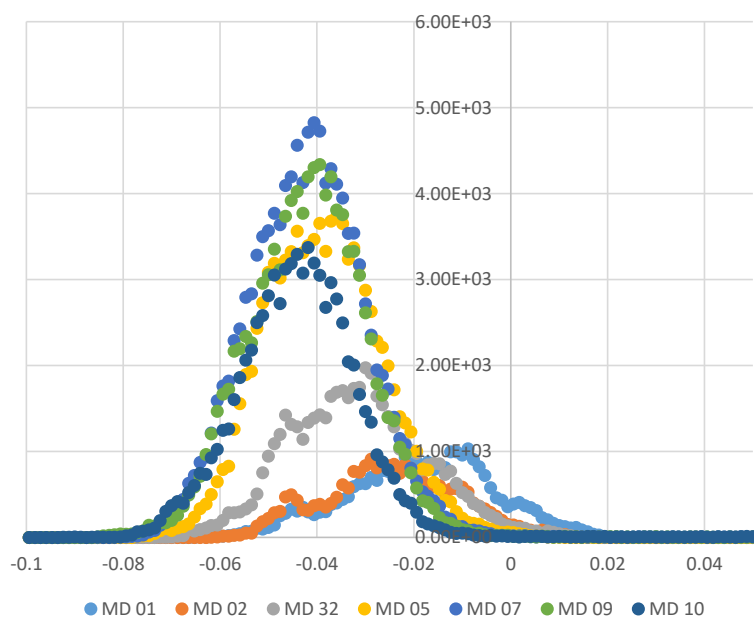


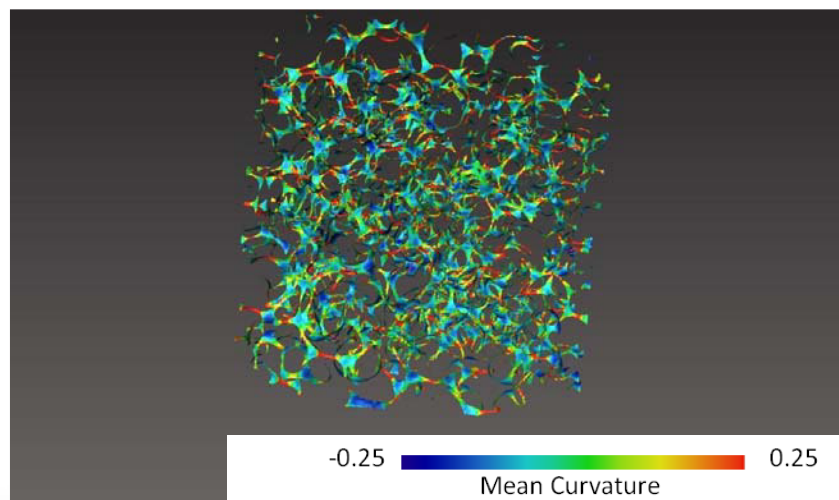
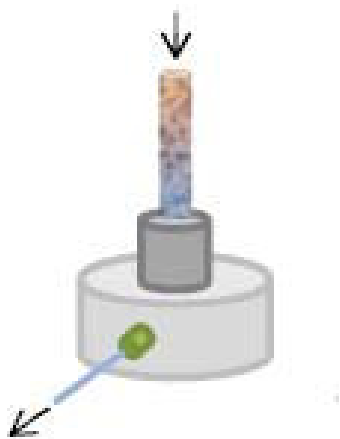


Main Drainage

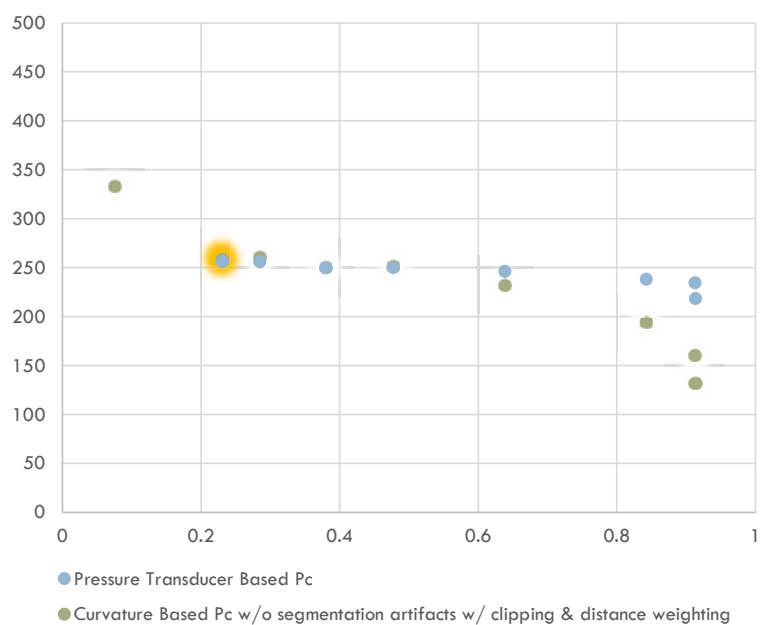


Mean Curvature Histogram

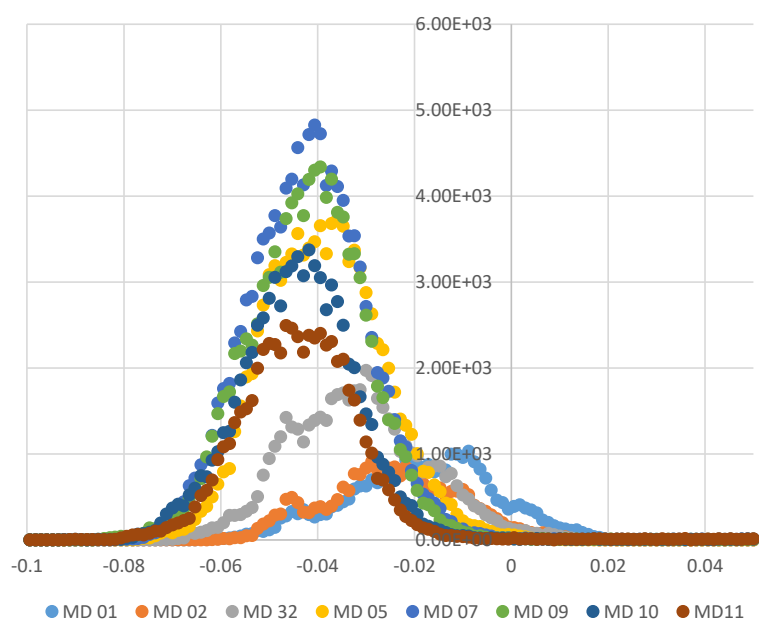


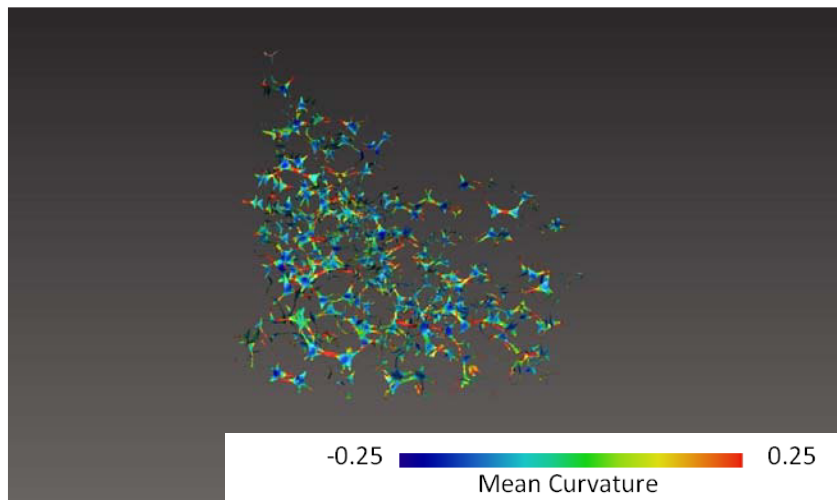
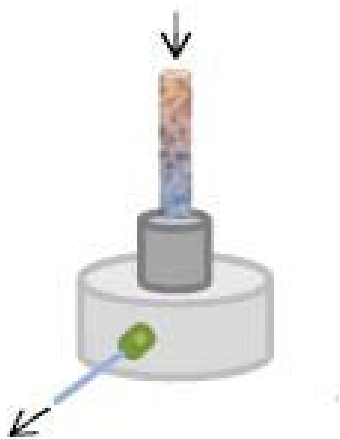


Main Drainage

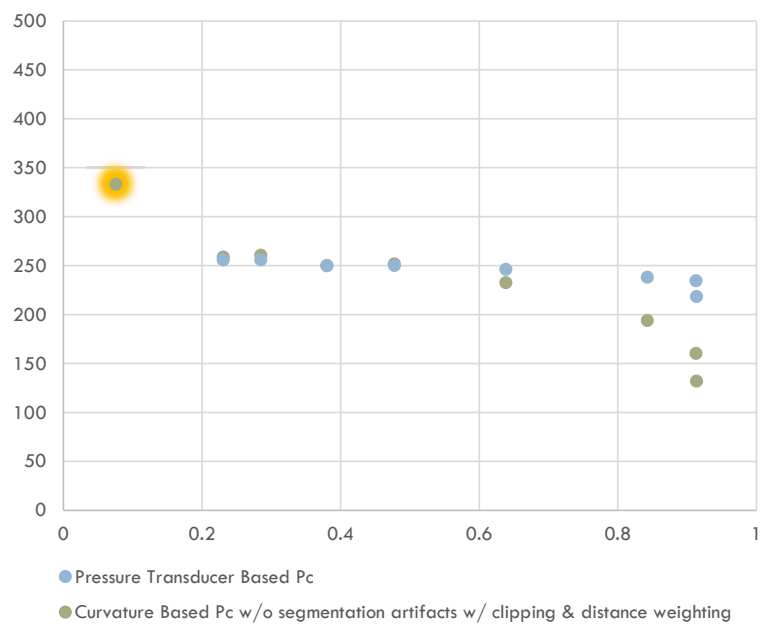


Mean Curvature Histogram

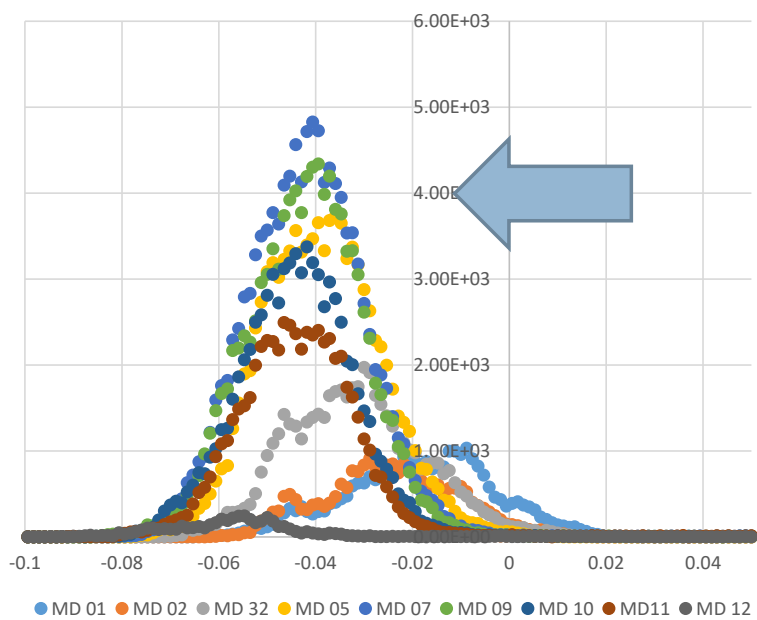




Main Drainage

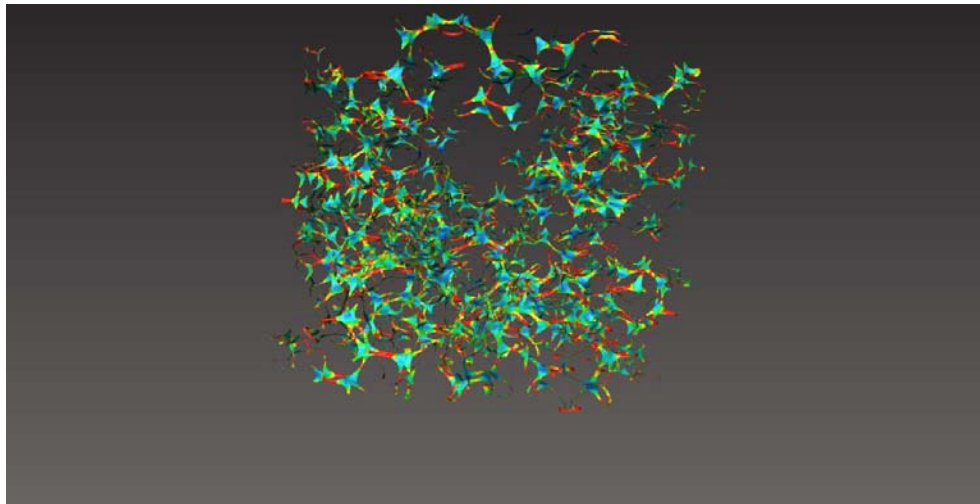


Mean Curvature Histogram

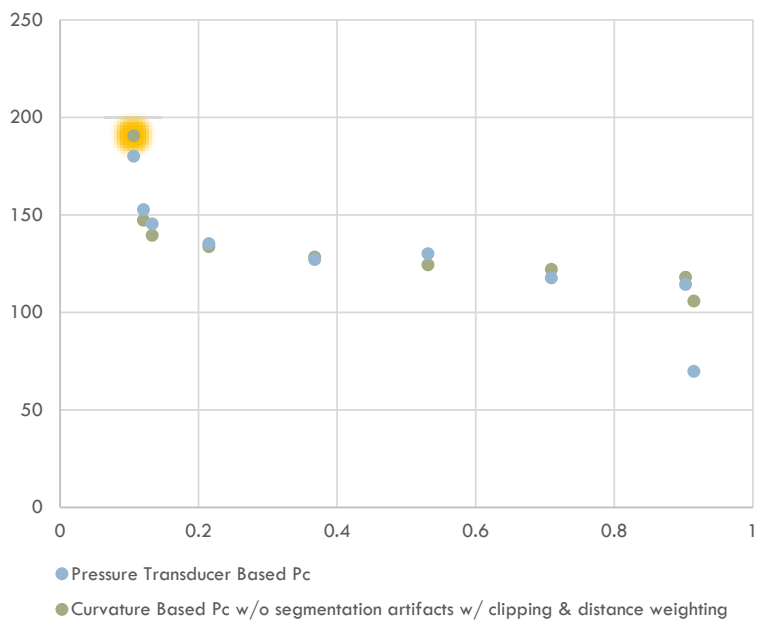


MAIN IMBIBITION

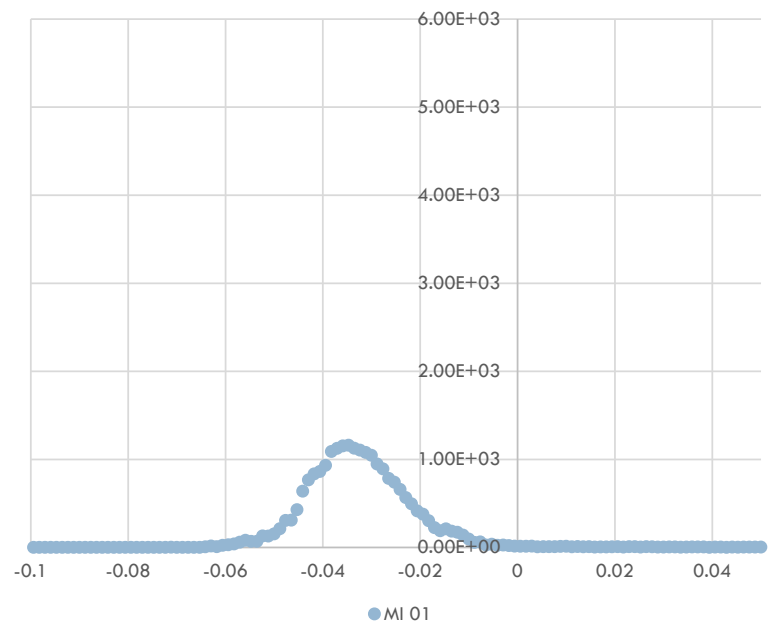
Connected phases

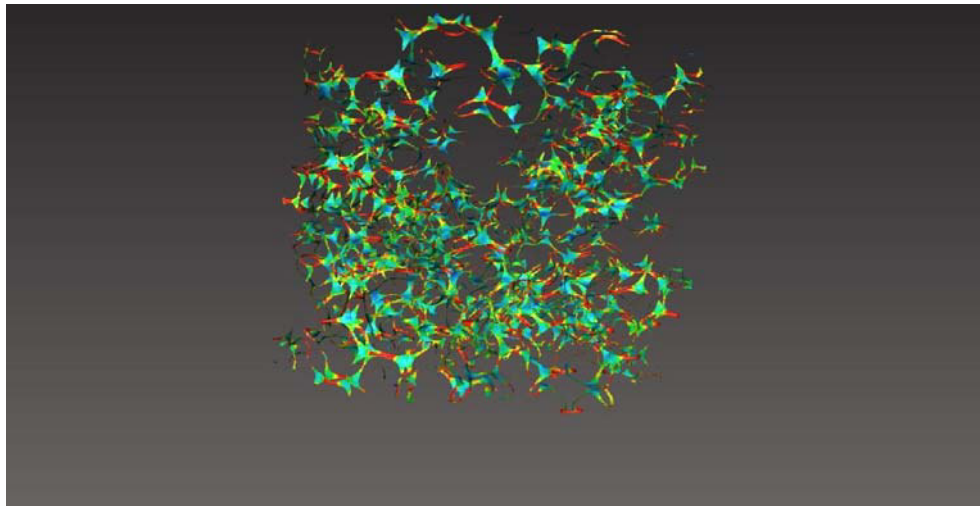


Main Imbibition

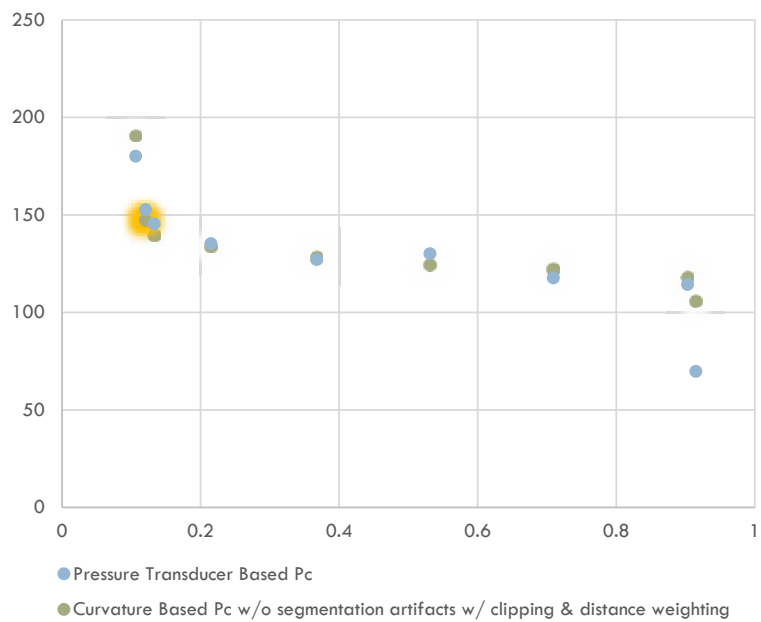


Mean Curvature Histogram

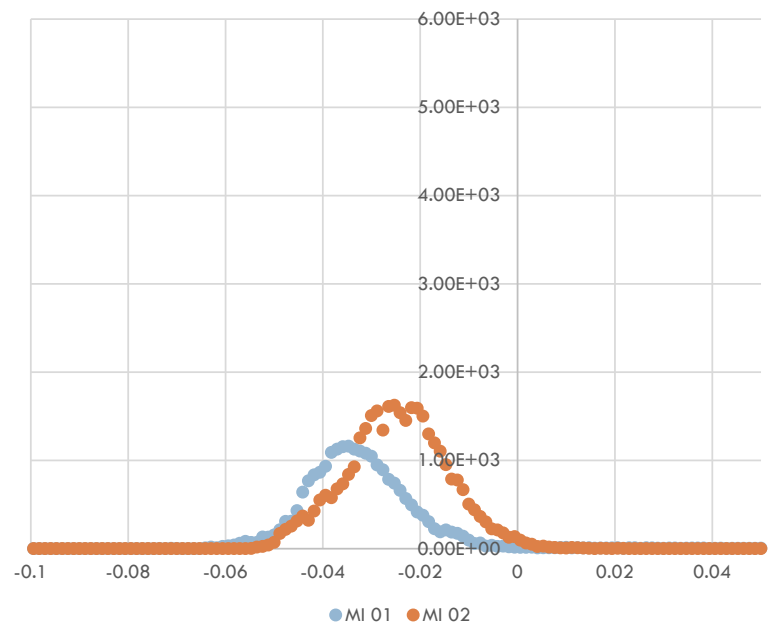


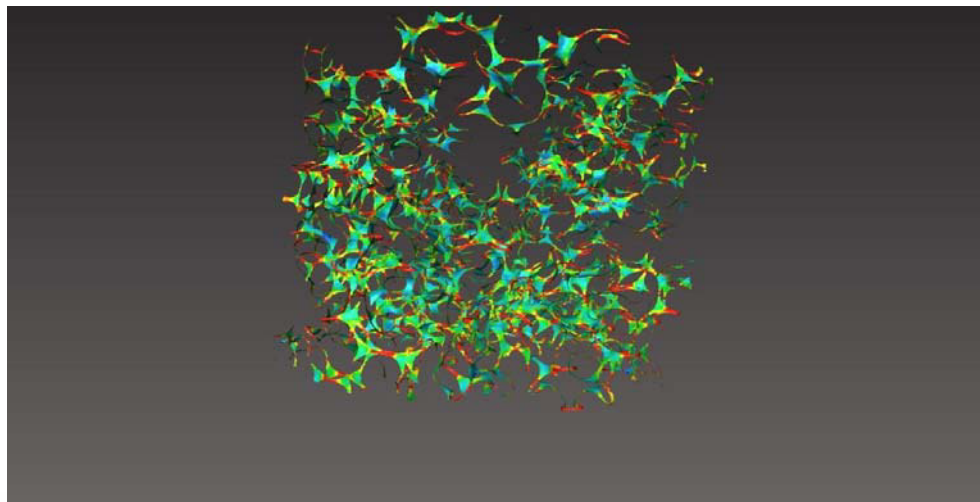


Main Imbibition

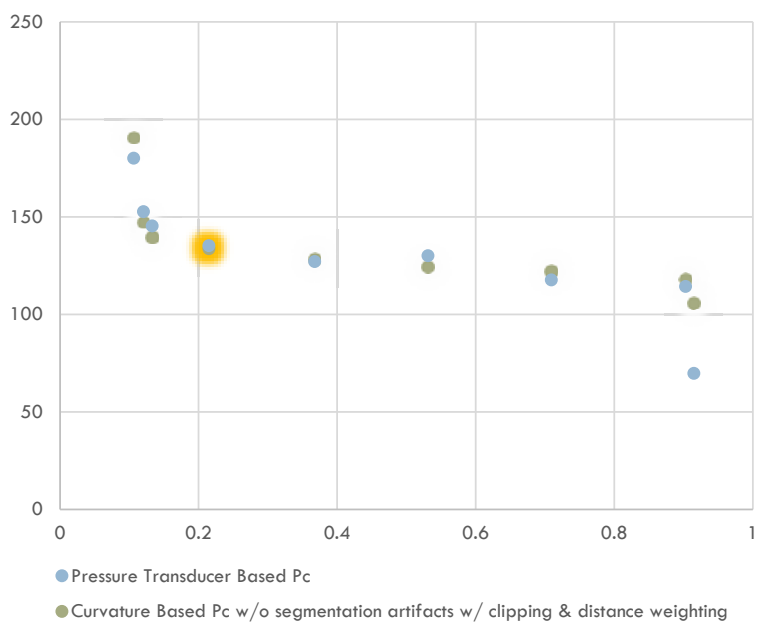


Mean Curvature Histogram

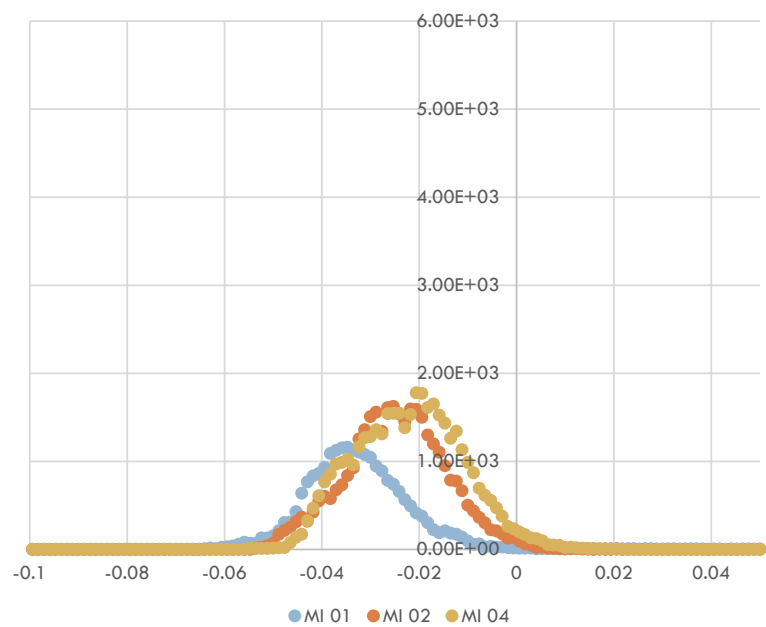


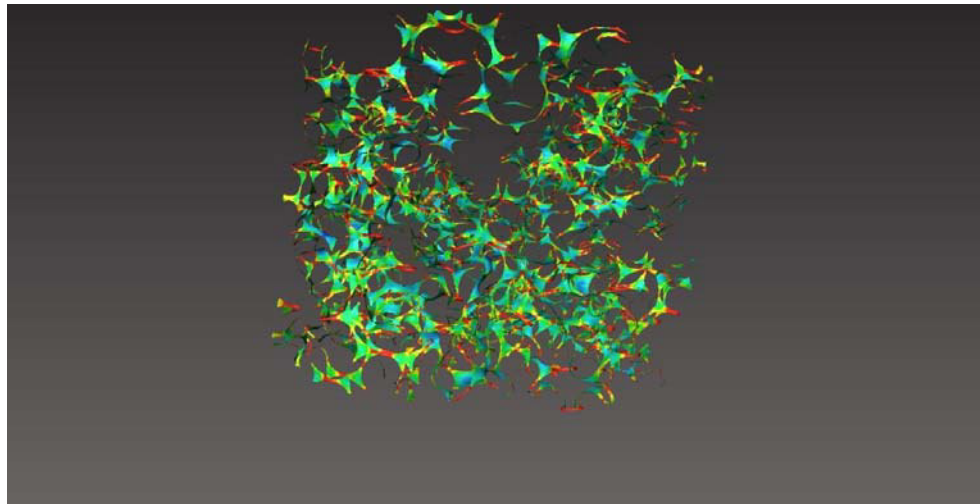


Main Imbibition

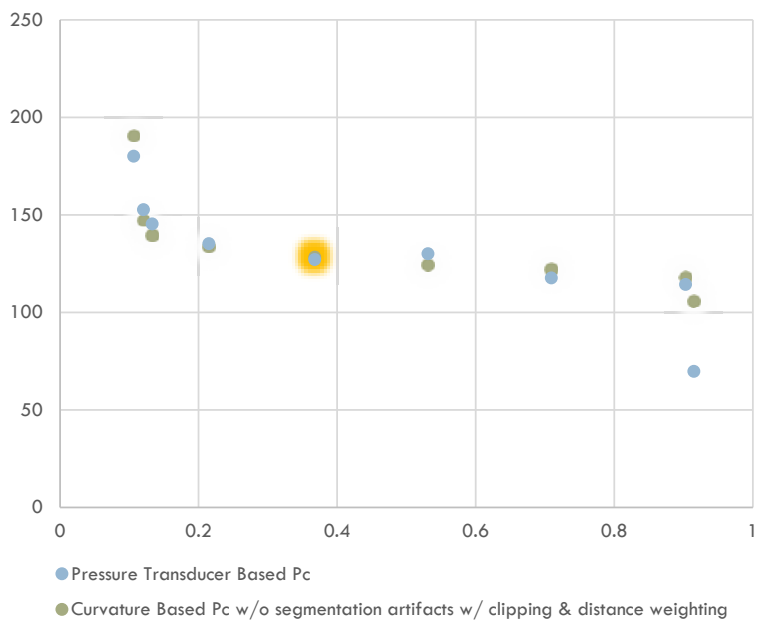


Mean Curvature Histogram

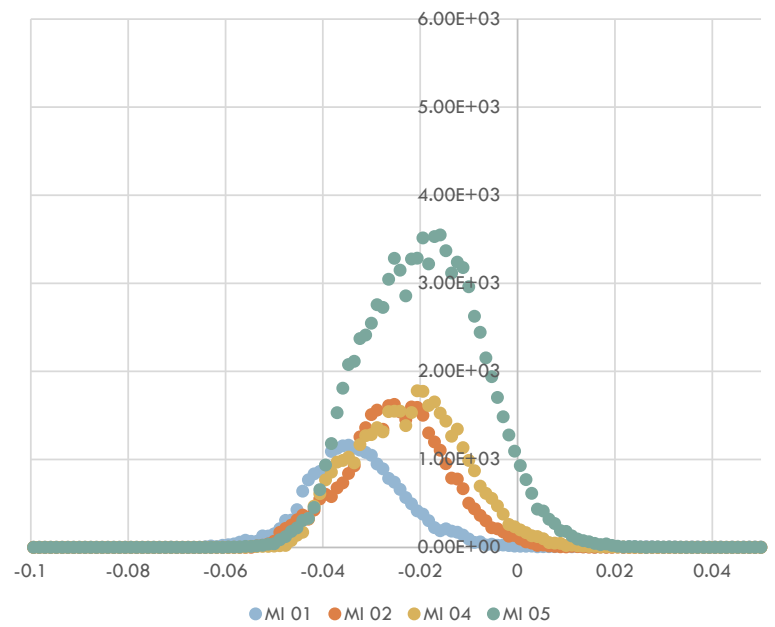


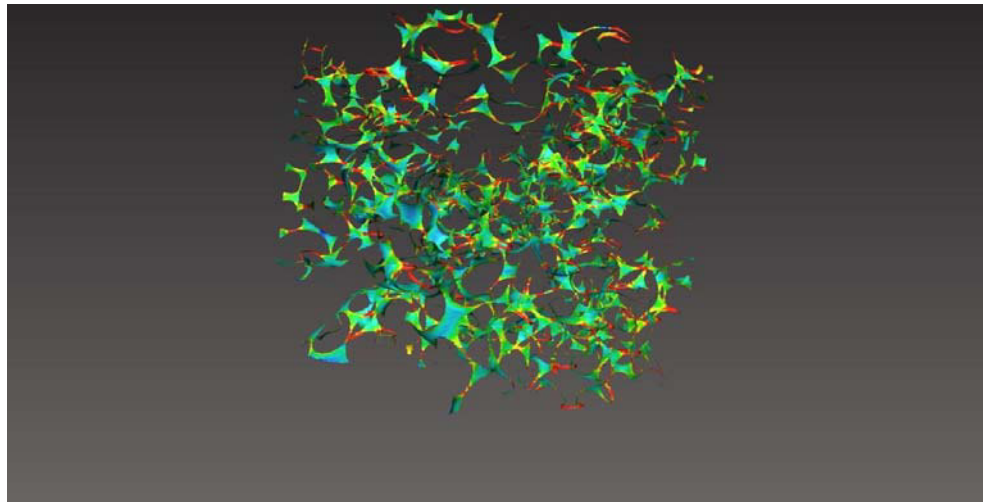


Main Imbibition

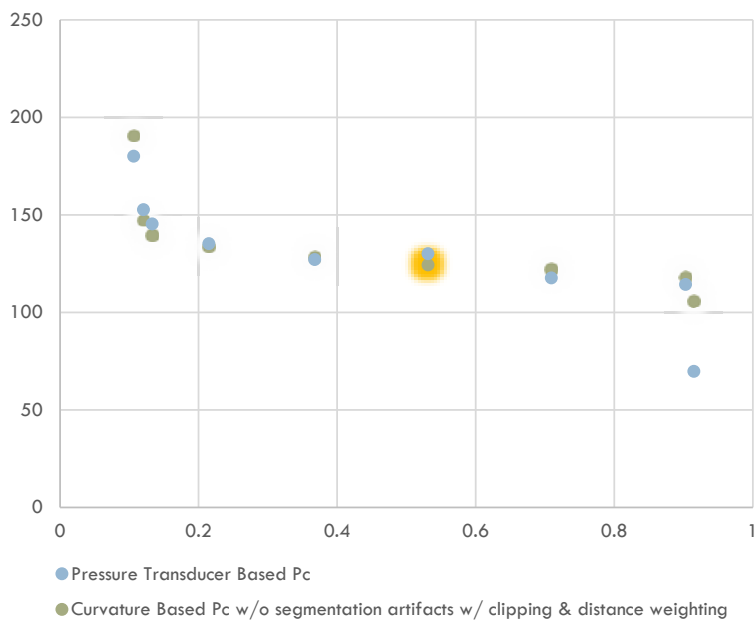


Mean Curvature Histogram

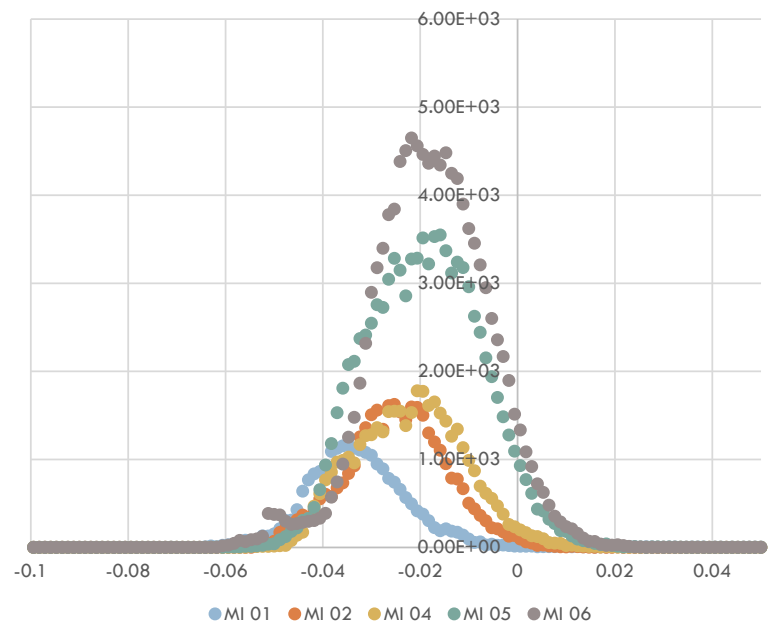


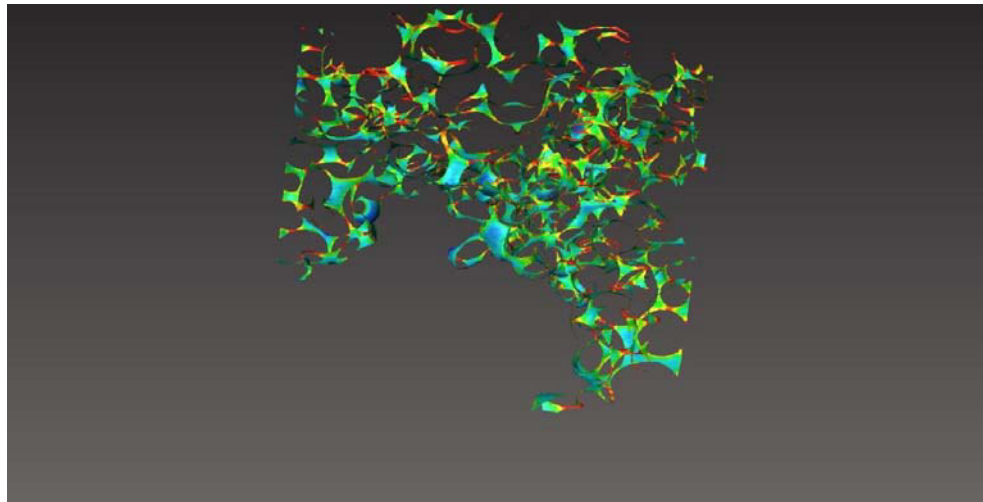


Main Imbibition

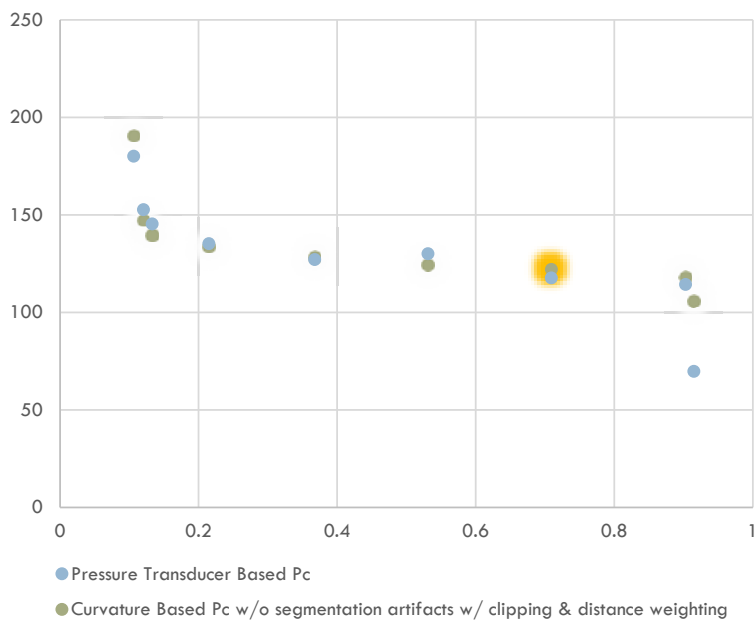


Mean Curvature Histogram

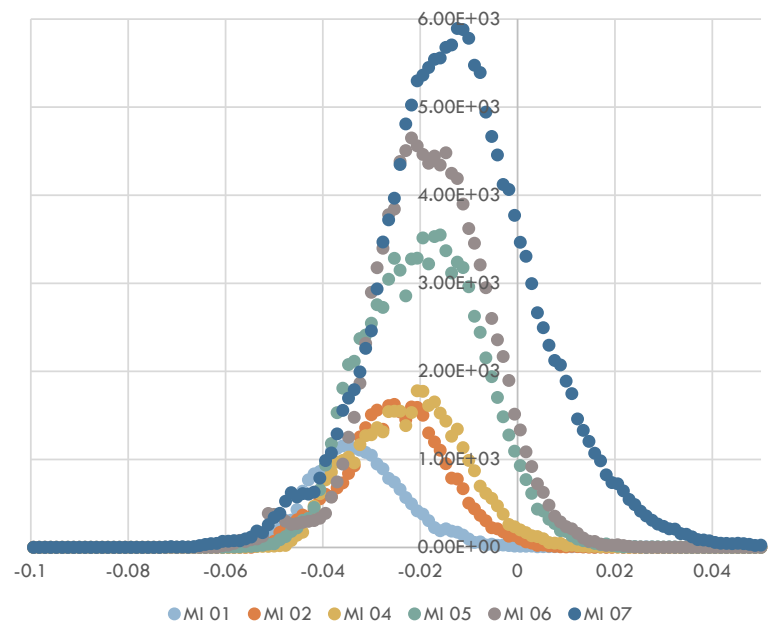


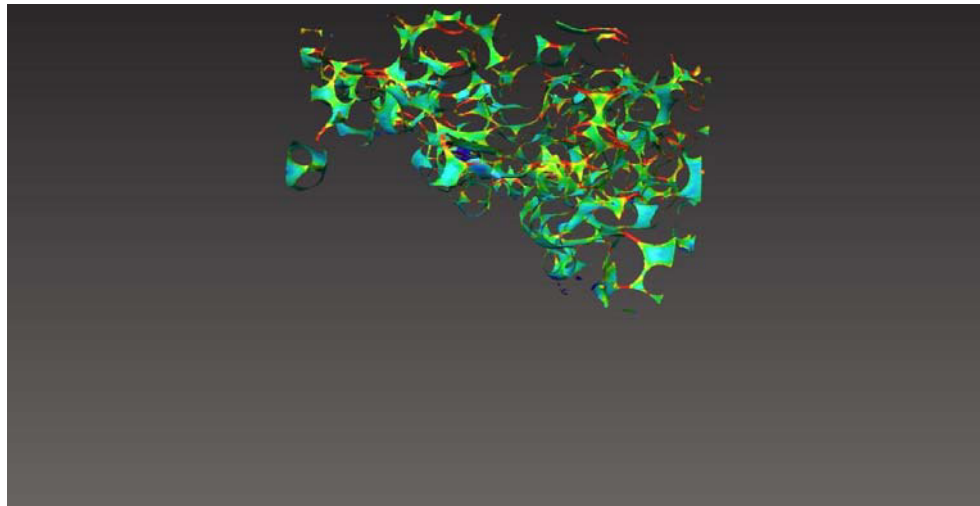


Main Imbibition

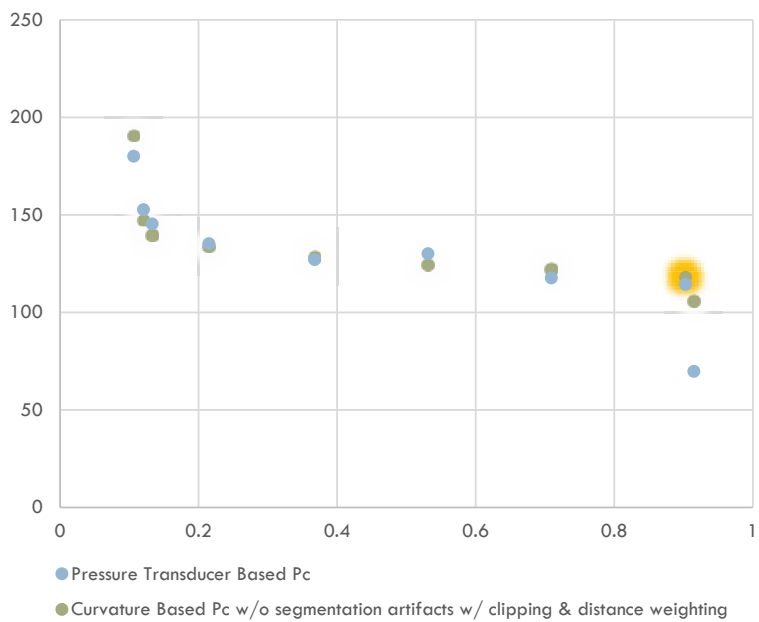


Mean Curvature Histogram

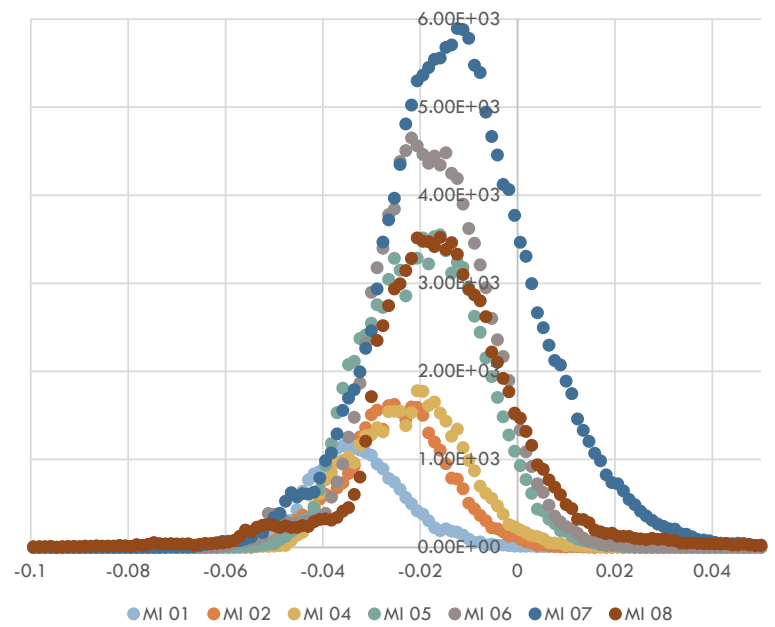


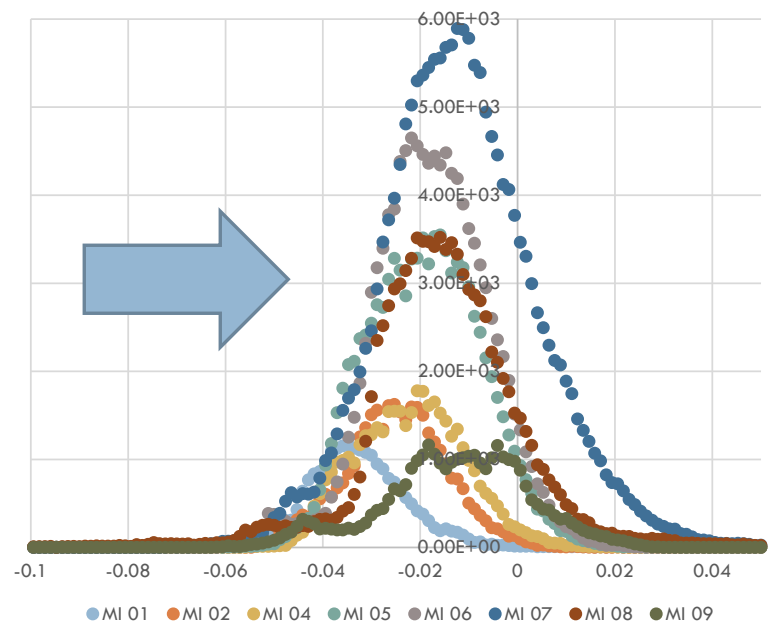
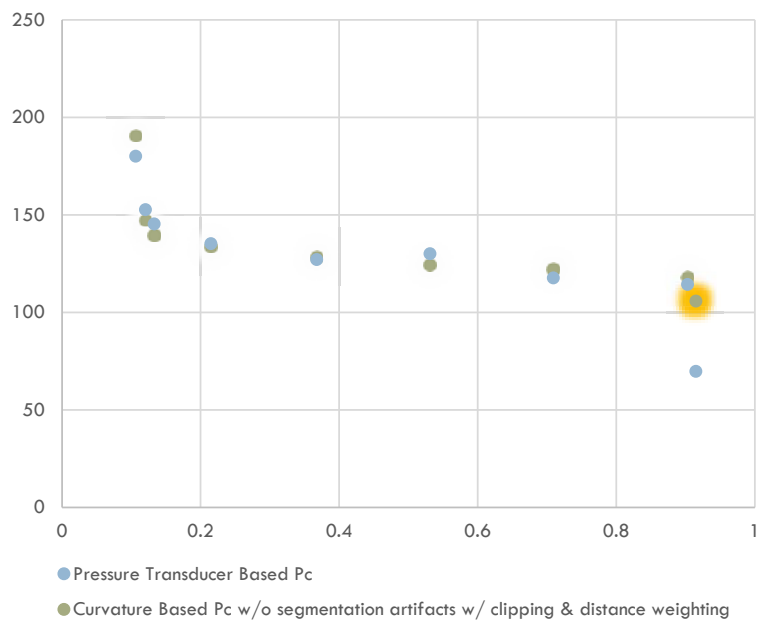
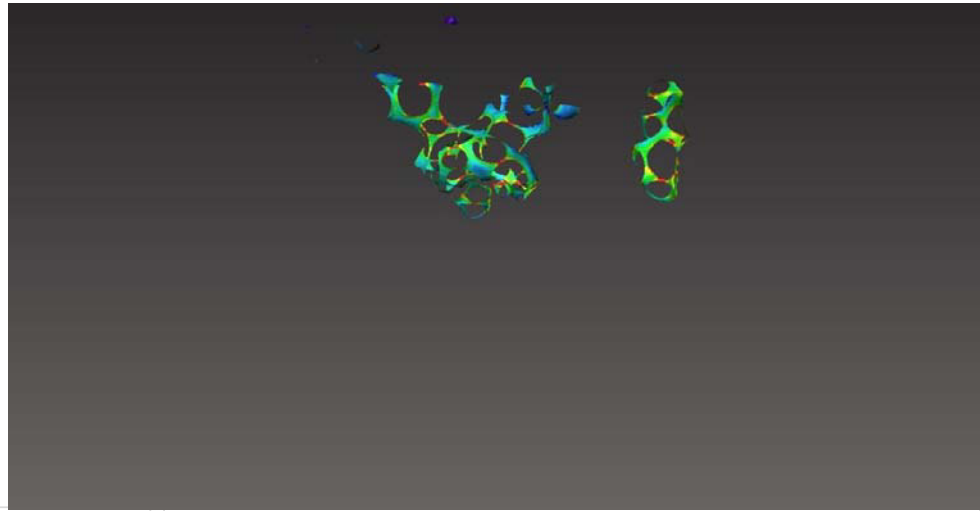


Main Imbibition



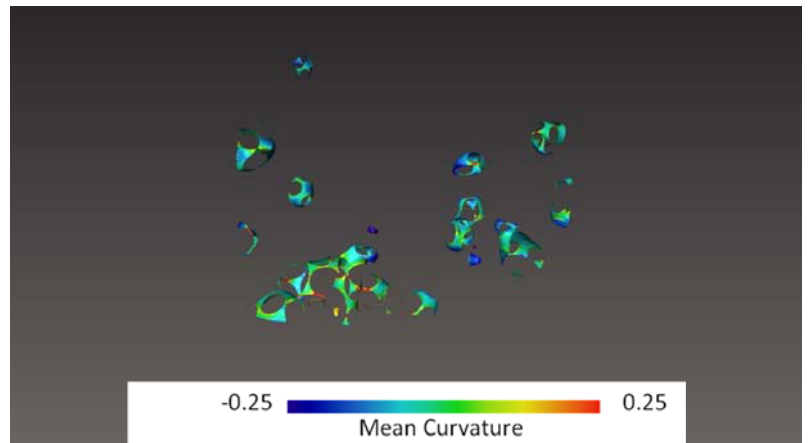
Mean Curvature Histogram



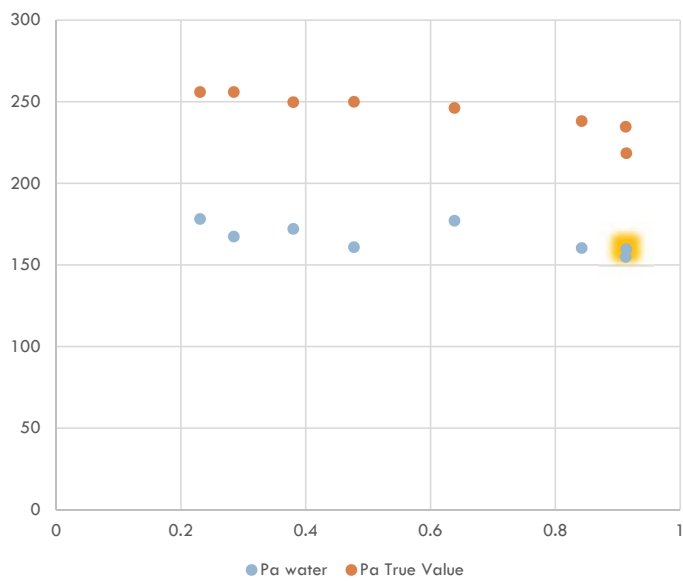


MAIN DRAINAGE

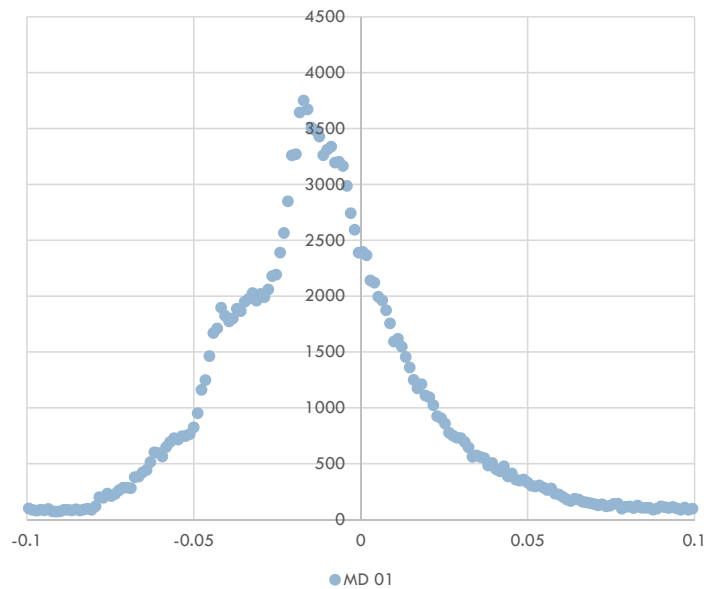
Disconnected nonwetting-connected wetting

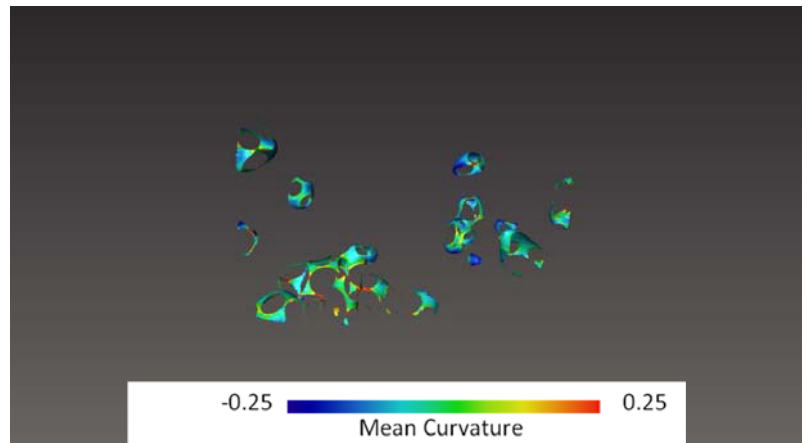


Main Drainage

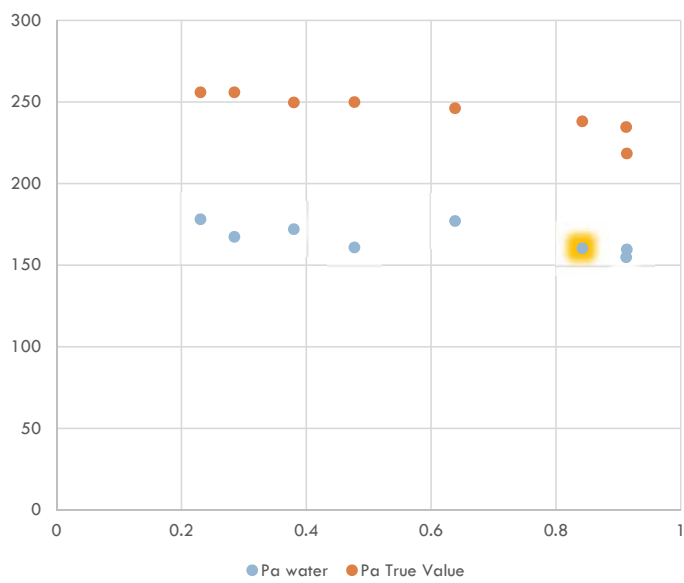


Mean Curvature Histogram

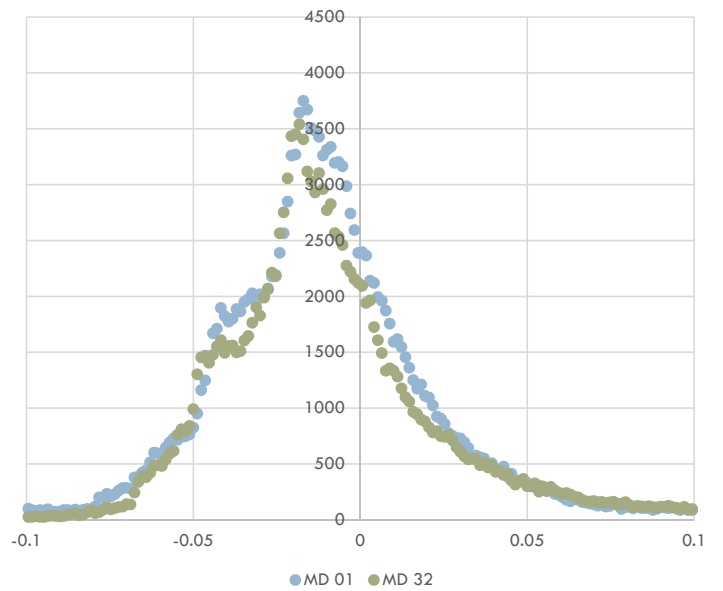




Main Drainage

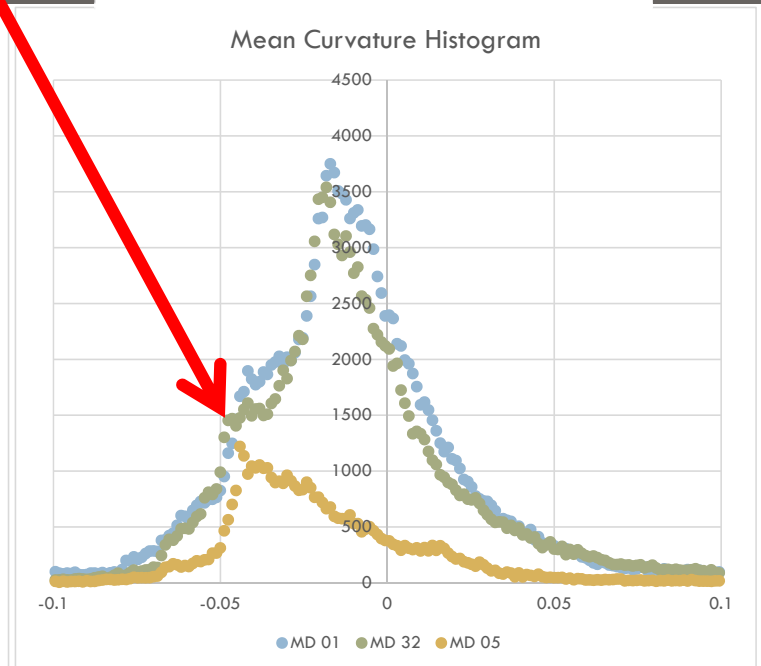
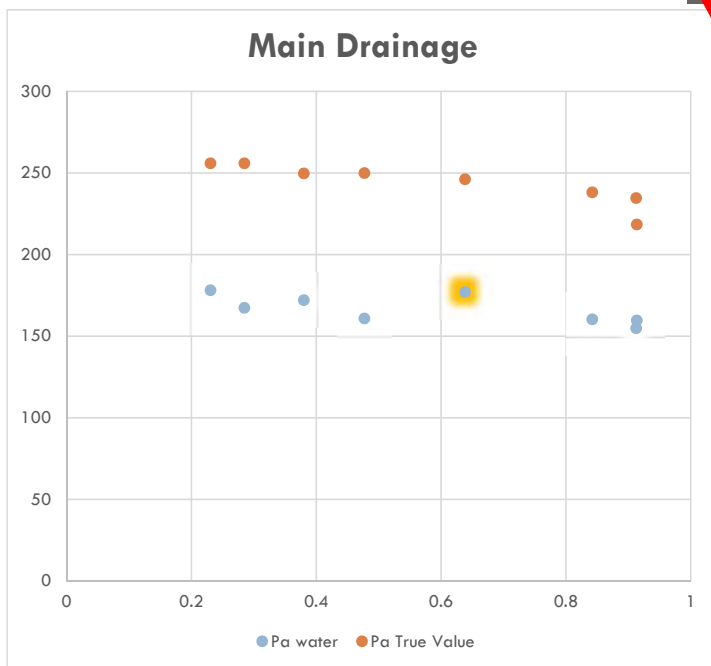
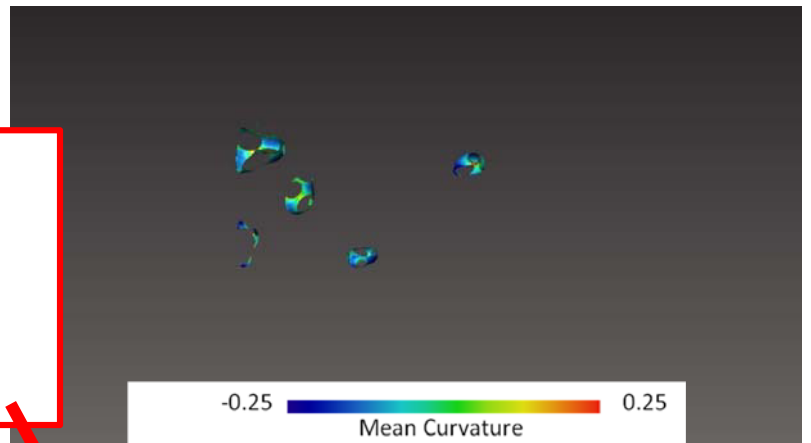


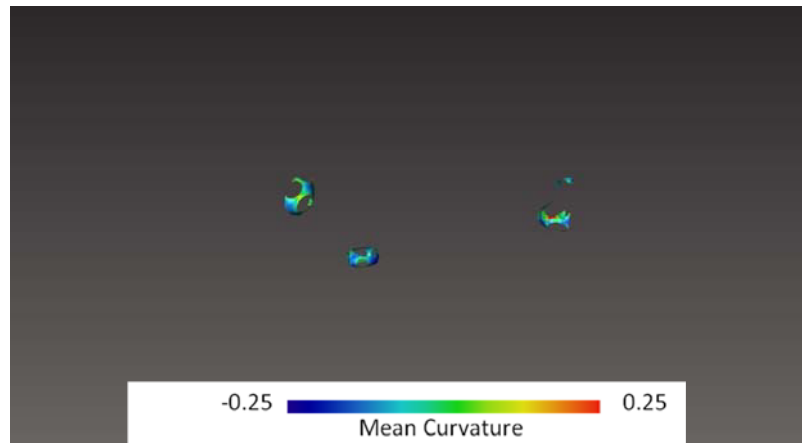
Mean Curvature Histogram



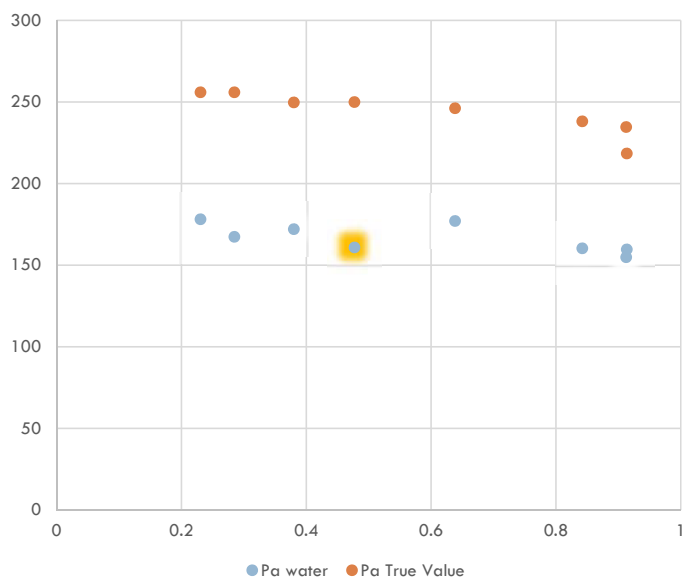


Multi-pore blobs of disconnected nonwetting phase are not sustained at higher capillary pressures

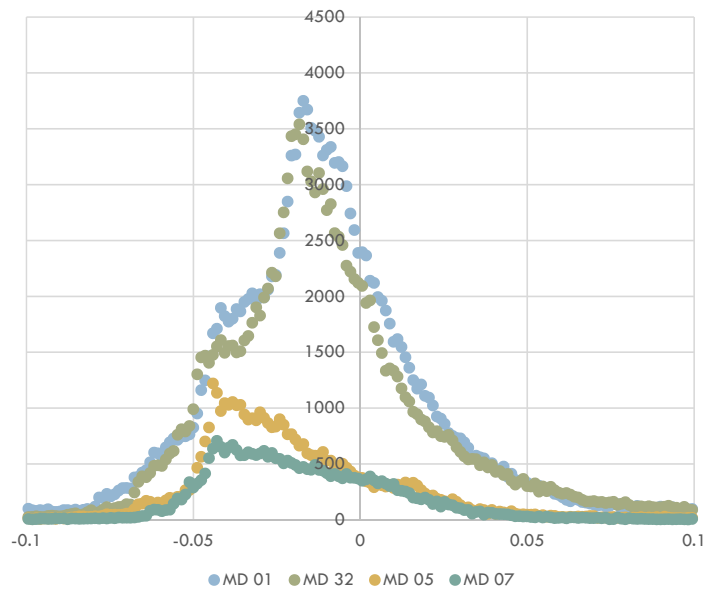


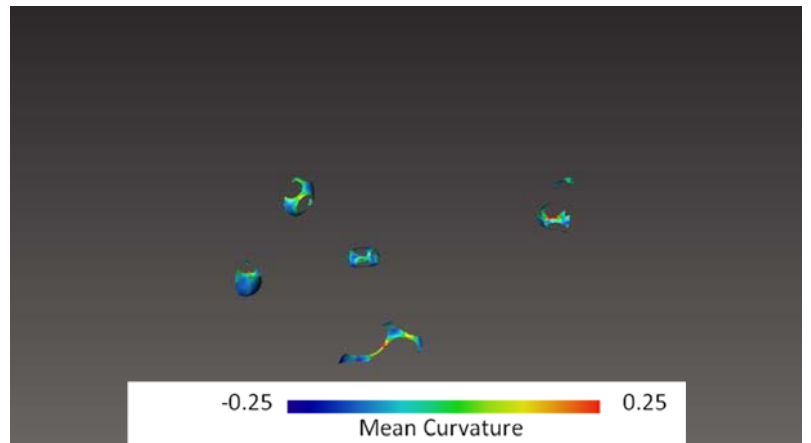


Main Drainage

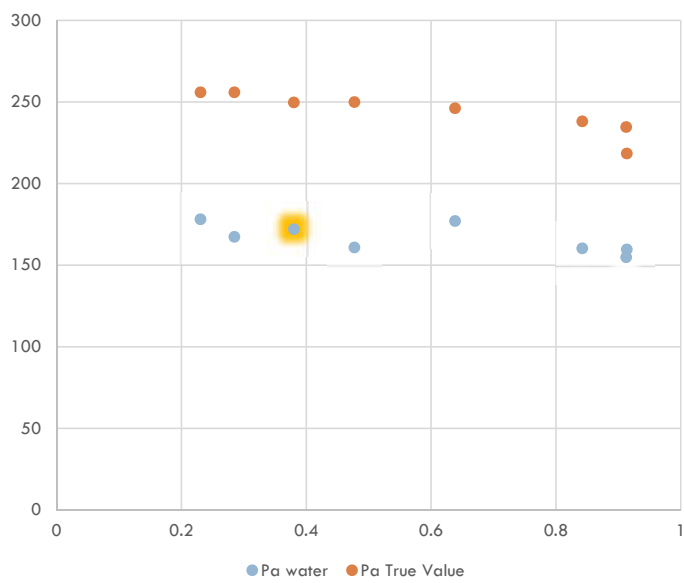


Mean Curvature Histogram

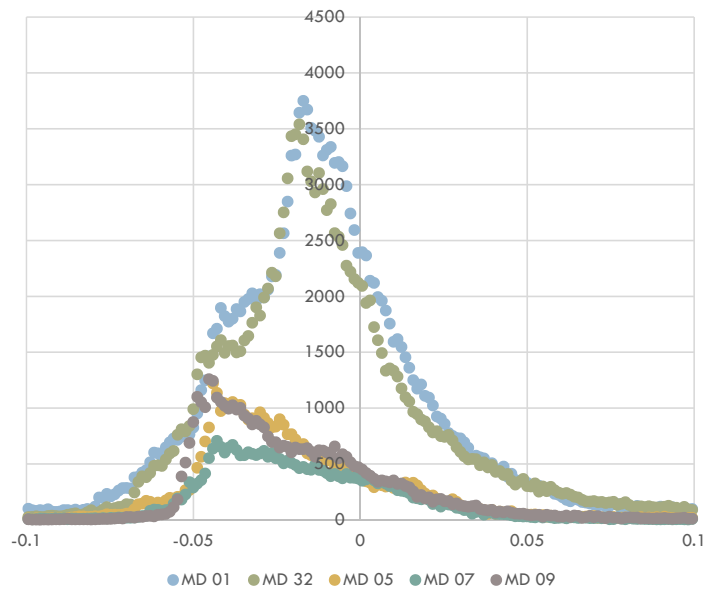


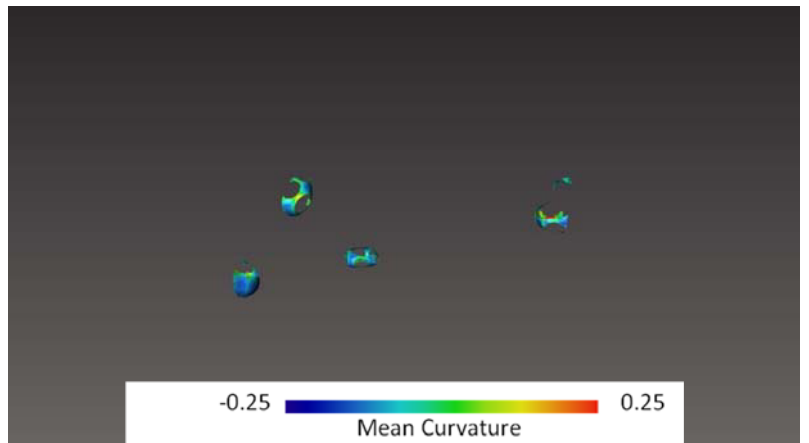


Main Drainage

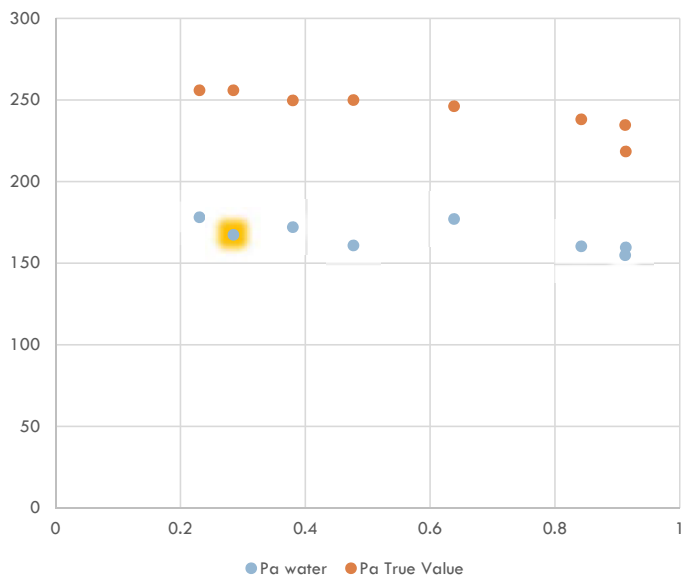


Mean Curvature Histogram

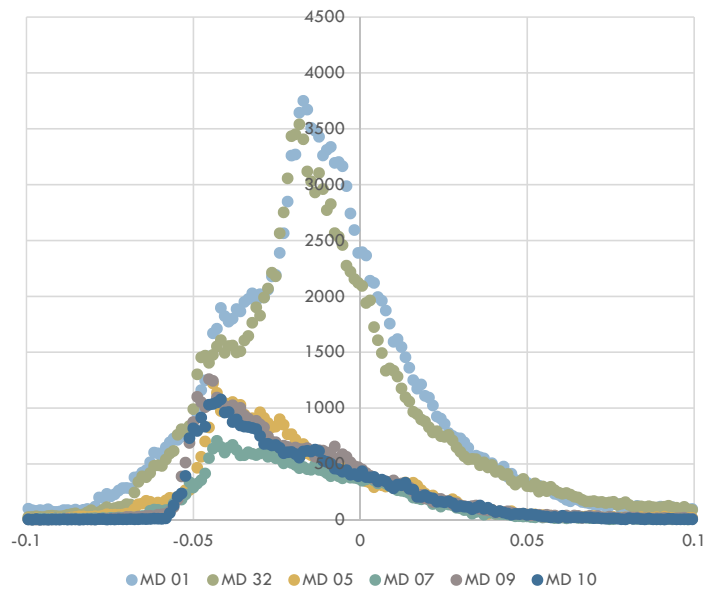


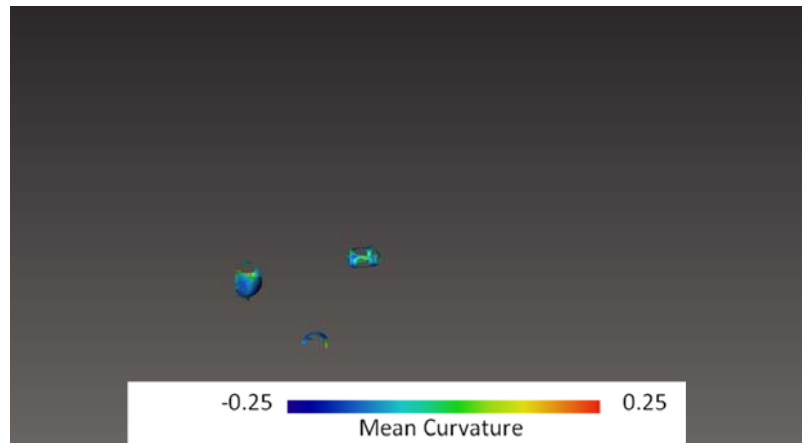


Main Drainage

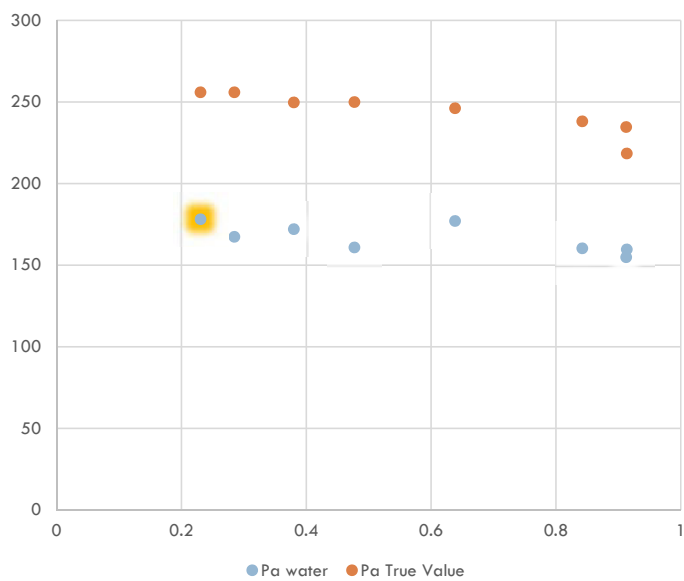


Mean Curvature Histogram

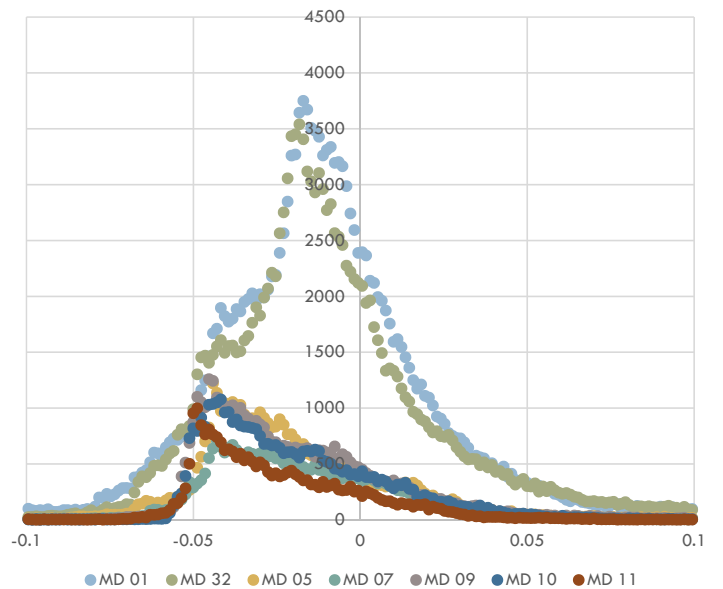




Main Drainage

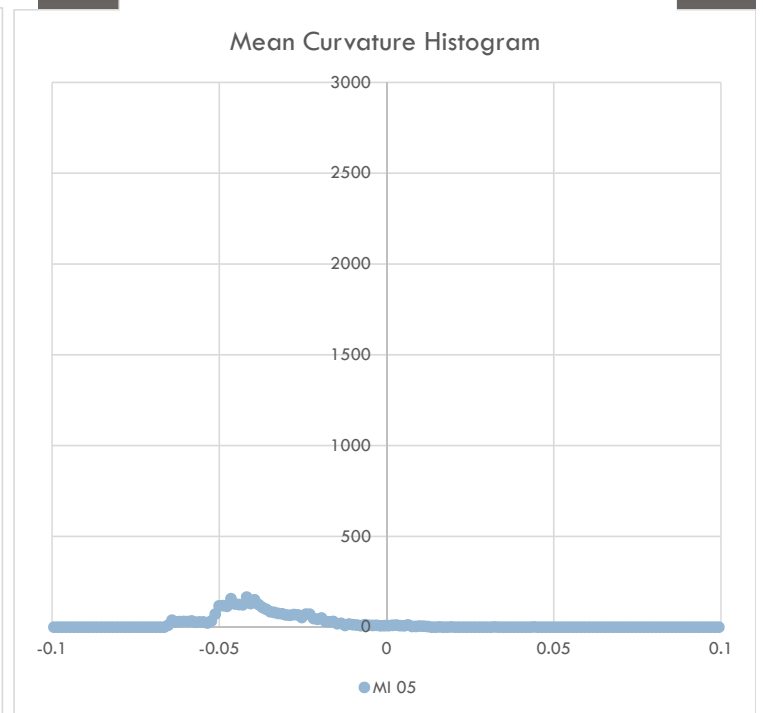
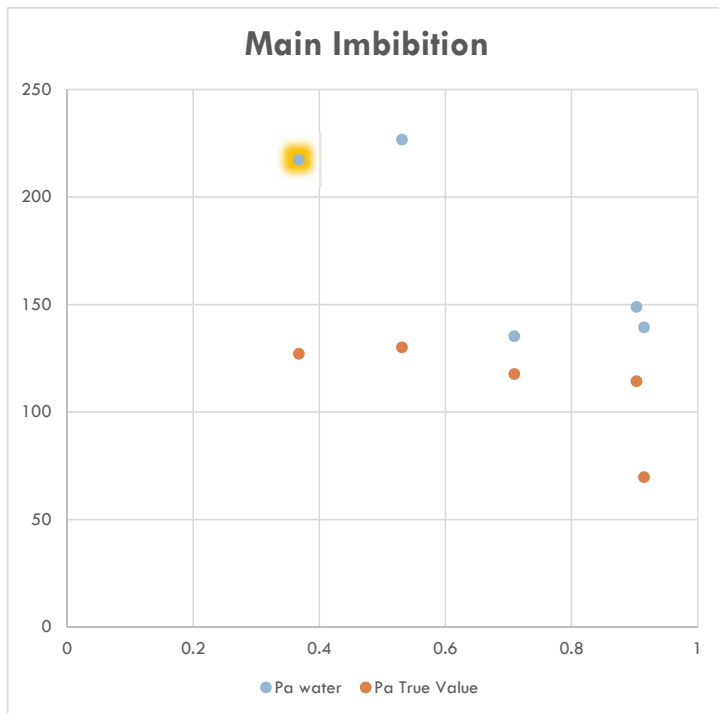
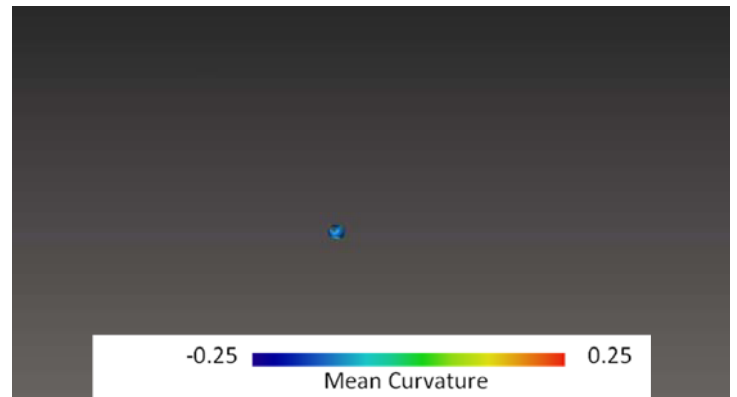


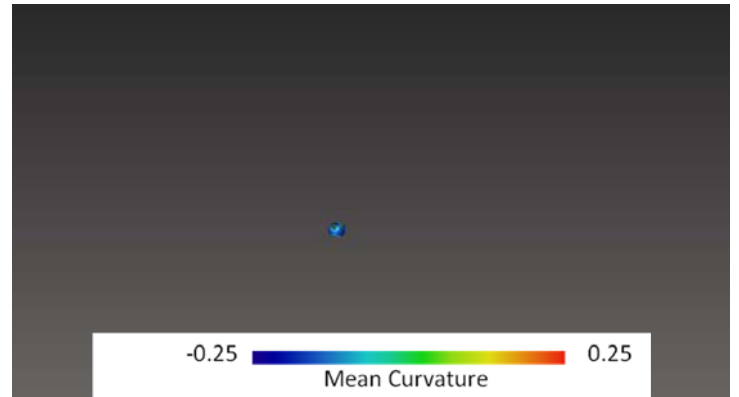
Mean Curvature Histogram



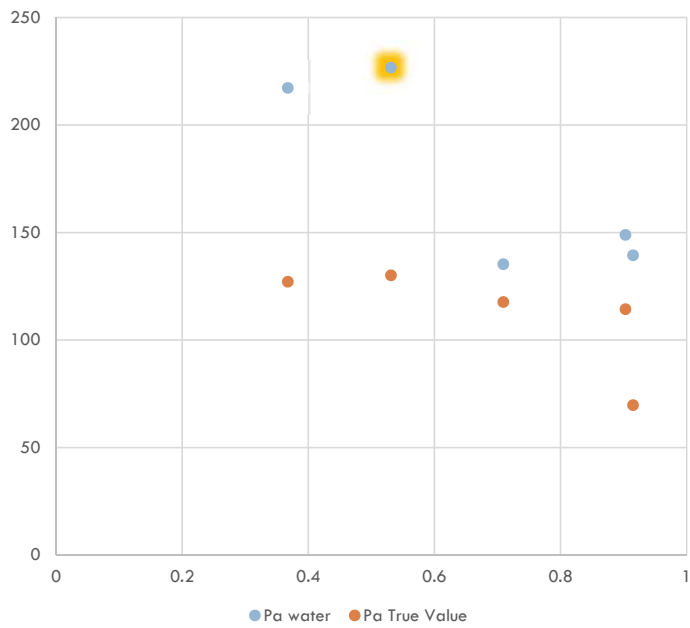
MAIN IMBIBITION

Disconnected nonwetting-connected wetting

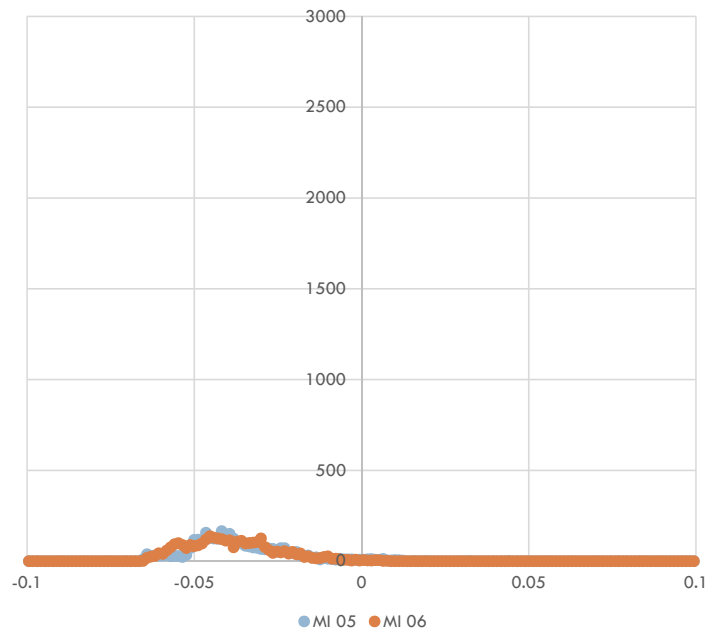


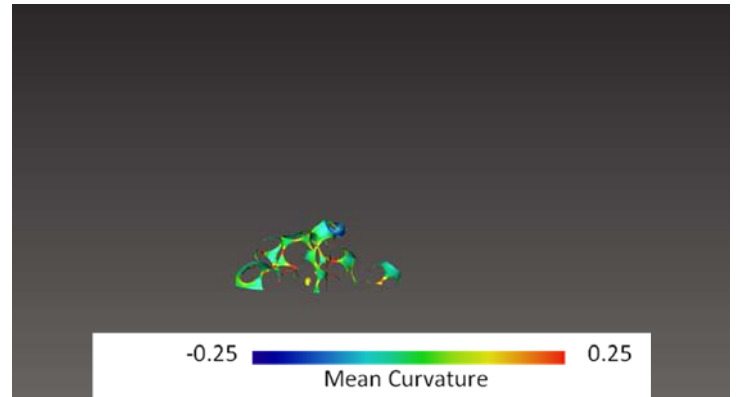


Main Imbibition

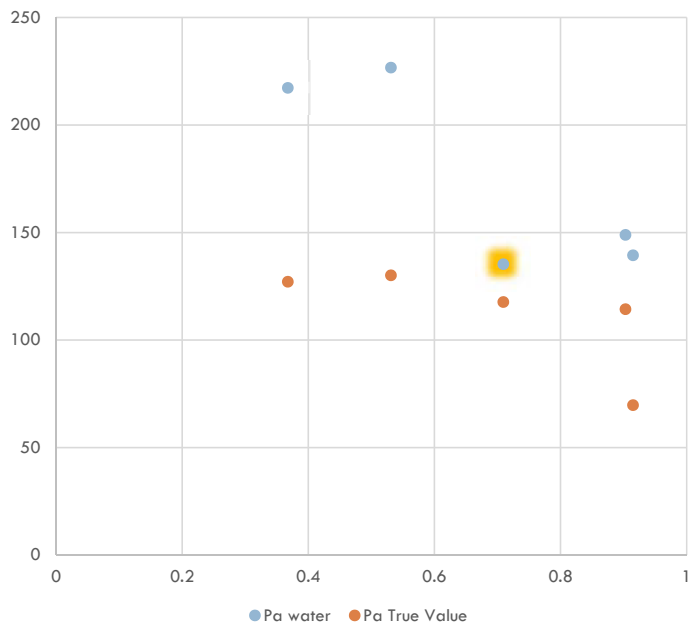


Mean Curvature Histogram

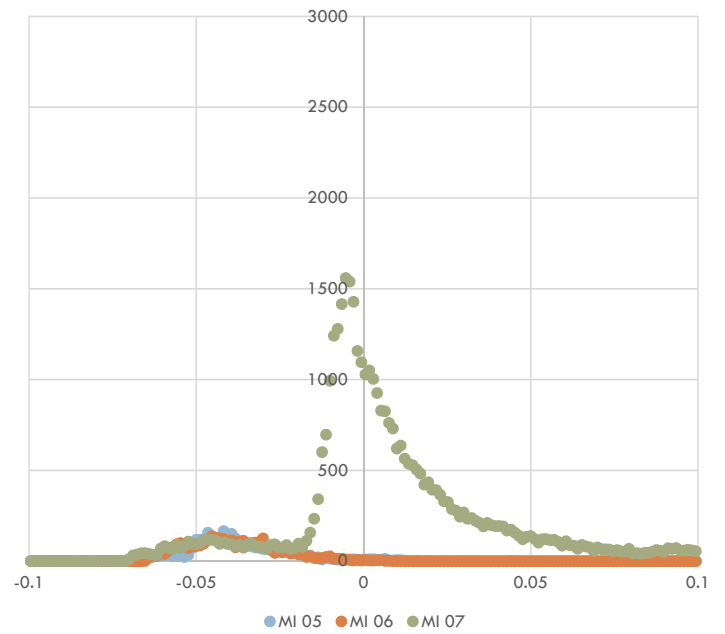


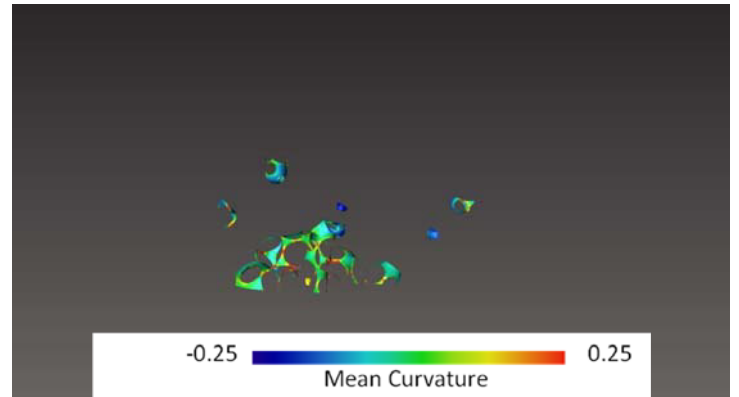


Main Imbibition

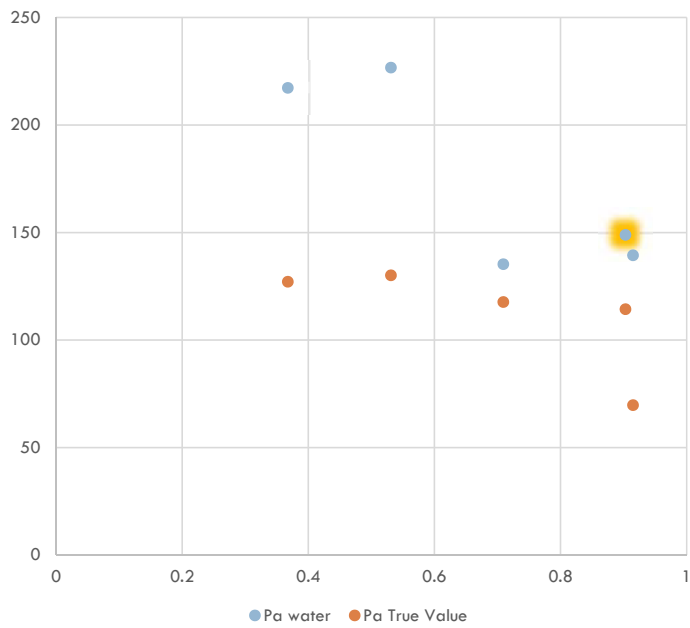


Mean Curvature Histogram

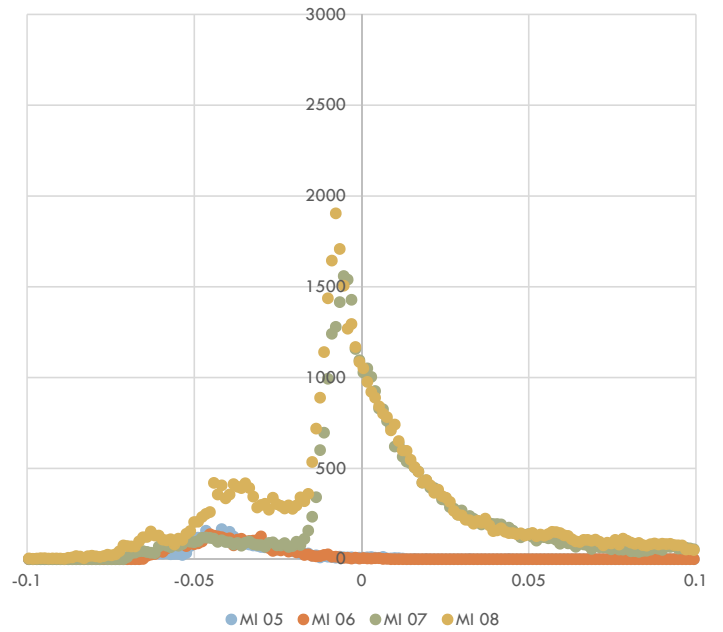




Main Imbibition



Mean Curvature Histogram





Generating more interface
at higher (previous) pressure
state

